



Geoscientific Model Development Discussions is the access reviewed
discussion forum of *Geoscientific Model Development*

Incorporation of the C-GOLDSTEIN efficient climate model into the GENIE framework: the “genie_eb_go_gs” configuration of GENIE

R. Marsh¹, A. Yool¹, R. J. Myerscough¹, N. R. Edwards², and J. G. Shepherd¹

¹National Oceanography Centre, University of Southampton, Waterfront Campus, European Way, Southampton SO14 3ZH, UK

²Department of Earth and Environmental Sciences, CESPAR, The Open University, Milton Keynes, UK

Received: 8 December 2008 – Accepted: 12 December 2008 – Published: 9 January 2009

Correspondence to: R. Marsh (rma@noc.soton.ac.uk)

Published by Copernicus Publications on behalf of the European Geosciences Union.

GMDD

2, 1–79, 2009

The “genie_eb_go_gs”
configuration of
GENIE

R. Marsh et al.

Title Page

Abstract

Introduction

Conclusions

References

Tables

Figures

◀

▶

◀

▶

Back

Close

Full Screen / Esc

Printer-friendly Version

Interactive Discussion



Abstract

A computationally efficient, intermediate complexity ocean-atmosphere-sea ice model (C-GOLDSTEIN) is incorporated into the Grid ENabled Integrated Earth system modeling (GENIE) framework. This involved decoupling of the three component modules that were re-coupled in a modular way, to allow replacement with alternatives and coupling of further components within the framework. The climate model described here (`genie_eb_go_gs`) is the most basic version of GENIE in which atmosphere, ocean and sea ice all play an active role. Compared to the original model, latitudinal grid resolution has also been generalized to allow a wider range of surface grids to be used and an altered convection scheme has been added. Some other minor modifications and corrections have been applied. For four default meshes, and using the same default parameters as far as possible, we present the results from spin-up experiments. Evaluation of equilibrium states in terms of composite model-observation errors is demonstrated, with caveats regarding the use of un-tuned key parameters. For each mesh, we also carry out four standard climate experiments, based on international protocols: (i) equilibrium climate response (sensitivity) to doubled atmospheric CO₂ concentration; (ii) transient climate response to CO₂ concentration, increasing at 1% per annum, until doubling; (iii) response of the Atlantic meridional overturning circulation to freshwater hosing over 100 years; and (iv) hysteresis of the overturning circulation under slowly-varied freshwater forcing. Climate sensitivity and transient climate response lie in the ranges 2.85–3.13°C and 1.67–1.97°C respectively. The Atlantic overturning collapses under 0.1 Sv hosing, and subsequently recovers, for one of the meshes. Hosing at 1.0 Sv, the overturning collapses, and remains collapsed, on all four meshes. The hysteresis experiments reveal a wide range in stability of the initial state, from strongly monostable to strongly bistable. The dependencies of experimental results on choice of mesh are thus highlighted and discussed.

GMDD

2, 1–79, 2009

The “`genie_eb_go_gs`” configuration of GENIE

R. Marsh et al.

[Title Page](#)

[Abstract](#)

[Introduction](#)

[Conclusions](#)

[References](#)

[Tables](#)

[Figures](#)

◀

▶

◀

▶

[Back](#)

[Close](#)

[Full Screen / Esc](#)

[Printer-friendly Version](#)

[Interactive Discussion](#)



1 Introduction

To model climate change on multi-millennial timescales, to fully explore model parameter space, or to run many scenarios for anthropogenic climate forcing, we need to use “Earth System Models” (ESMs) which include all the necessary components and processes (e.g., atmosphere, ocean, sea-ice, and for some purposes ice sheets, biogeochemical cycles, and for “deep time” palaeoclimate studies changes in geography, orography and bathymetry). The models must however be computationally much faster than the general circulation models that are used to simulate climate change on shorter (centennial) timescales, such models being much too slow for these purposes. A new 5 generation of such ESMs of Intermediate Complexity (EMICs) has emerged in recent years (Claussen et al., 2002). In EMICs, computational speed is achieved through a combination of simplified physics, low resolution and efficient numerics (e.g., asynchronous coupling, implicit time-stepping). EMICs have been used operationally to explore long-term climate change and commitment (IPCC, 2007a), and for a variety of 10 palaeoclimate studies (e.g., IPCC, 2007b). Plattner et al. (2008) found no systematic difference in predictions between EMICs and higher-complexity models.

A new framework for Earth System Modelling has been developed, based on Grid technology, in the Grid-ENabled Integrated Earth system model (GENIE) framework which is both flexible and scaleable in complexity. At the present time, the framework 20 supports two main levels of complexity (dimensionality and physics) in the atmosphere, GENIE-1 and GENIE-2 (see Lenton et al., 2007), and several levels of spatial resolution. The present paper describes the most basic GENIE-1 model, originally known as C-GOLDSTEIN (Edwards and Marsh, 2005, henceforth EM05), the code of which has been modified for incorporation into the GENIE framework as `genie_eb_go_gs`, or 25 strictly, `genie_ea_go_gs`, according to the naming convention for model instances defined by Lenton et al. (2007) (see Sect. 6). Further advantages of the GENIE structure include the availability of grid-based tools for launching and analysing experiments, and version-control tools including automatic testing of the code and any modifica-

The “`genie_eb_go_gs`” configuration of GENIE

R. Marsh et al.

[Title Page](#)

[Abstract](#)

[Introduction](#)

[Conclusions](#)

[References](#)

[Tables](#)

[Figures](#)

◀

▶

◀

▶

[Back](#)

[Close](#)

[Full Screen / Esc](#)

[Printer-friendly Version](#)

[Interactive Discussion](#)



tions. These general GENIE tools are described elsewhere (see GENIE wiki pages at <http://source.ggy.bris.ac.uk/wiki/GENIE>).

The purpose of this paper is to provide a basic description of the model components and their coupling, with minor updates of hitherto published descriptions. We also outline four default meshes, and present selected results obtained in spin-up experiments with each. This is followed by some practical examples of four standard climate experiments, again with each mesh. We focus on the `genie_eb_go_gs` instance of GENIE, pointing out where and how it compares to C-GOLDSTEIN and to the related Bern3D model of Müller et al. (2006). The following sections outline in practical detail: Model Components; Meshes and Timesteps; Constants, Parameters and Prescribed Inputs; Control Run Climatologies; Standard Climate Experiments. In summary and discussion, we emphasize the “unique selling points” of GENIE, and GENIE-1 in particular.

2 Model components

2.1 Ocean

“GOLDSTEIN”, from Global Ocean-Linear Drag Salt and Temperature Equation Integrator, is a 3-D frictional-geostrophic ocean model based on the reduced physics of the thermocline equations. The basic equations and a single-basin configuration are described in Edwards et al. (1998). A global ocean version which constitutes a precursor to GOLDSTEIN was introduced in Edwards and Shepherd (2002) with idealised global geography and resolution intermediate between box models and resolved models. The present version of GOLDSTEIN is essentially as described in EM05, with a few modifications (see below). Various improvements to the ocean physics (surface and bottom mixed layer schemes; a semi-free surface; a more general equation of state; options for running under mixed boundary conditions, and a more sophisticated diapycnal mixing scheme) are in progress and will be documented in future papers.

Velocities and fluxes are non-dimensionalized in GOLDSTEIN. The sign convention

GMDD

2, 1–79, 2009

The “`genie_eb_go_gs`” configuration of GENIE

R. Marsh et al.

[Title Page](#)

[Abstract](#)

[Introduction](#)

[Conclusions](#)

[References](#)

[Tables](#)

[Figures](#)

◀

▶

◀

▶

[Back](#)

[Close](#)

[Full Screen / Esc](#)

[Printer-friendly Version](#)

[Interactive Discussion](#)



for the transfer of vertical fluxes of heat and moisture between modules is positive into the ocean. The dynamical variables of GOLDSTEIN are potential temperature and salinity anomaly (relative to a reference salinity – see Table 3). In summary, the following physical processes are explicitly represented:

- 5 – Horizontal and vertical transport of heat, salinity anomaly, and other specified tracers (biogeochemical, passive), through advection, convection and mixing (horizontal, vertical and isoneutral, the latter optional on compiling with the “-diso” option)
- 10 – Surface exchange of heat with the atmosphere and sea ice, according to the local balance of incoming shortwave radiation, sensible and latent heat fluxes, and outgoing long-wave radiation
- Surface exchange of moisture with the atmosphere, sea ice and land, according to balance of precipitation, evaporation, runoff (at coastal gridpoints) and sea ice freezing/melting
- 15 – Surface input of momentum from prescribed winds

The density of seawater (ρ) is a function of temperature (T) and salinity (S), according to the simplified equation of state:

$$\rho = 1000 + (0.7968S) - (0.0559T) - (0.0063T^2) + (3.7315 \times 10^{-5}T^3) \quad (1)$$

This closely approximates the UNESCO formula for observed ocean density in kg m^{-3}
20 if S is in practical salinity units and T in degrees Celsius (Winton and Sarachik, 1993)
but neglects the non-linear effects due to compressibility.

We have incorporated four separate modifications relative to the original GOLD-
STEIN model of EM05, two of which are options which generalize the application to
different grids and geographies, while two represent minor but significant improvements
25 to the dynamics:

The “genie_eb_gs” configuration of GENIE

R. Marsh et al.

[Title Page](#)

[Abstract](#)

[Introduction](#)

[Conclusions](#)

[References](#)

[Tables](#)

[Figures](#)

◀

▶

◀

▶

[Back](#)

[Close](#)

[Full Screen / Esc](#)

[Printer-friendly Version](#)

[Interactive Discussion](#)



5

10

15

20

25

- The implementation now allows for the calculation of barotropic flow around multiple islands (disconnected land-masses). As noted in EM05, barotropic flow around islands, and hence through straits, can be calculated from the solution of a set of linear constraints arising from the integration of the depth-averaged momentum equations around each island. Barotropic flows through Bering Strait and the Indonesian Throughflow have significant effects on the modern global circulation.
 - A wider variety of horizontal mesh structure and resolution can now be accommodated, as the model now allows an arbitrary latitudinal distribution of gridpoints. The original code assumed equal spacing in sine of latitude (equal area cells), whereas the new code simply requires that the increment of sine(latitude) varies smoothly with latitude. In particular, constant spacing in degrees is now possible.
 - The direct convection scheme of Müller et al. (2006) has been implemented as an optional addition to the standard scheme. In essence this moves fluid directly from unstable upper layers to their level of neutral density, moving fluid sequentially upwards through the column to maintain volume conservation, but otherwise not mixing the intervening fluid. In principle, this should improve water mass properties. When this option is activated, the algorithm is iterated until the upper layer is stably stratified, then the original scheme is applied to ensure stability in the rest of the column, if required.
 - An adjustment has been made to the upstream weighting coefficients in the advection scheme that originally did not consistently take account of the grid curvature. The upstream weighting is an approximation of the Fiadeiro and Veronis (1977) scheme – see Müller et al. (2006) for details.
- In addition to these modifications, a scaling error in the parameters of the equation of state was discovered and corrected in June 2006. The error was a hard-coded scaling for density variation in the equation of state, which was not updated when changing

The “genie_eb_go_gs” configuration of GENIE

R. Marsh et al.

[Title Page](#)

[Abstract](#)

[Introduction](#)

[Conclusions](#)

[References](#)

[Tables](#)

[Figures](#)

◀

▶

◀

▶

[Back](#)

[Close](#)

[Full Screen / Esc](#)

[Printer-friendly Version](#)

[Interactive Discussion](#)



the depth scale (e.g. from 4 km to 5 km). The overall effect of this correction was a 25% increase in the dimensional values of wind, currents, overturning, diffusivities and inverse timescales.

2.2 Atmosphere

- 5 The Energy Moisture Balance Model (EMBM) of the atmosphere is based closely on that of the UVic Earth System Model (Weaver et al., 2001), essentially as described in EM05, with two exceptions (see below).

In the EMBM, vertical fluxes are in SI units, while horizontal velocities and fluxes, which are calculated using a modified form of the ocean and sea-ice transport code,
10 are non-dimensionalized. The sign convention for vertical fluxes of heat and moisture is positive into the atmosphere. The dynamical variables of the EMBM are atmospheric surface temperature and specific humidity. In summary, the following physical processes are explicitly represented:

- 15 – Horizontal transport of heat and moisture in atmosphere by winds and mixing
– Surface exchange of heat with ocean, sea ice and land, according to balance of incoming shortwave radiation, sensible and latent heat fluxes, and outgoing long-wave radiation, as a function of planetary albedo and radiative gases (CO_2 , water vapour)
20 – Surface exchange of moisture with the ocean, sea ice and land, according to the balance of precipitation, evaporation and (when the land surface module is not coupled) runoff, the latter through instantaneous reallocation of precipitation over land to coastal gridboxes according to simple representation of catchments (see Fig. 1)

Two changes have been incorporated since we originally described the EMBM in EM05:

The “genie_eb_go_gs” configuration of GENIE

R. Marsh et al.

[Title Page](#)

[Abstract](#)

[Introduction](#)

[Conclusions](#)

[References](#)

[Tables](#)

[Figures](#)

◀

▶

◀

▶

[Back](#)

[Close](#)

[Full Screen / Esc](#)

[Printer-friendly Version](#)

[Interactive Discussion](#)



5 – Seasonality has been accommodated by allowing the momentum and tracer fluxes to the ocean to change at each timestep. However, in the `genie.eb.go_gs` configuration, seasonally-varying wind forcing fields are not set up as a standard option, as they are in the Bern3D version of the ocean model. Thus the standard setup only has varying insolation forcing. The seasonal cycle of insolation is included by default in GENIE (compiling with the “-dosc” option in “genie-embm/src/fortran/makefile”). Incoming shortwave radiation is computed for each latitude and radiative forcing timestep (through the annual cycle), using modern day parameters for eccentricity (0.0167), sine of obliquity (0.397789), and precession (1.352631).

10 – The precipitation scheme has been modified to improve precipitation rates over continents when the simple land scheme of Williamson et al. (2006) is included, by relaxing specific humidity towards a relative humidity threshold rather than applying it instantaneously. However, the optimal relaxation timescale has been found to be close to one timestep, thus in the absence of the full land surface scheme, at least, differences are minimal.

2.3 Sea ice

The thermodynamic, advection-diffusion, sea-ice model is based on that implemented in the UVic Earth System Model (Weaver et al., 2001), and is as described in EM05.

15 – The sea-ice transport scheme has been modified to use the same implicit timestep formulation as is used for the atmospheric transport. This can be necessary when small grid spacing is used. A more sophisticated sea-ice scheme (including an Elastic-Viscous-Plastic rheology) has also been incorporated into the GENIE framework, and will be documented in a future paper.

20 – In the sea-ice model, vertical fluxes are in SI units, while horizontal fluxes are non-dimensionalized. The sign convention for vertical fluxes of heat and fresh water is positive into sea ice. The dynamical variables are sea-ice concentration (fractional

The “`genie.eb.go_gs`” configuration of GENIE

R. Marsh et al.

[Title Page](#)

[Abstract](#)

[Introduction](#)

[Conclusions](#)

[References](#)

[Tables](#)

[Figures](#)

◀

▶

◀

▶

[Back](#)

[Close](#)

[Full Screen / Esc](#)

[Printer-friendly Version](#)

[Interactive Discussion](#)



coverage of a grid box) and thickness. In summary, the following physical processes are explicitly represented:

- Horizontal transport of sea-ice concentration and thickness
- Surface exchange of heat with the atmosphere, according to the balance of incoming shortwave radiation, sensible and latent heat fluxes, and outgoing long-wave radiation
- Exchange of heat with ocean, according to the balance of sensible and latent heat fluxes (freezing/melting)
- Surface exchange of freshwater between the atmosphere and ocean. Precipitation is assumed to pass straight to the ocean, ignoring ice, and sublimed water from the ocean surface is added directly to the atmosphere
- Exchange of freshwater with the ocean, according to balance of freezing and melting

The freezing point for seawater (T_f) is a function of surface salinity (S_o) according to the formula of Millero (1978):

$$T_f = -0.0575S_o + 0.0017S_o^{3/2} - 0.0002S_o^2 \quad (2)$$

where S_o is in practical salinity units.

3 Coupling

Coupling between components is controlled by a set of inputs and output variables, which are exchanged as common arrays. Inputs to the ocean from the atmosphere are: air temperature ($^{\circ}\text{C}$); specific humidity (g kg^{-1}); wind speed (m s^{-1}); wind stress (N m^{-2}). The only output from the ocean to the atmosphere is sea-surface temperature

The “genie_eb_go_gs” configuration of GENIE

R. Marsh et al.

[Title Page](#)

[Abstract](#)

[Introduction](#)

[Conclusions](#)

[References](#)

[Tables](#)

[Figures](#)

◀

▶

◀

▶

[Back](#)

[Close](#)

[Full Screen / Esc](#)

[Printer-friendly Version](#)

[Interactive Discussion](#)



(°C). Inputs to the ocean from sea ice are: ice fraction; ice temperature (°C); ice thickness (m). Outputs from the ocean to sea ice are: upper level temperature (°C), salinity (psu) and current (m s^{-1}).

In addition to atmosphere-ocean exchanges, inputs to the atmosphere from the land surface scheme of Williamson et al. (2006) are: surface temperature (°C) and soil moisture (m water equivalent). Note that in C-GOLDSTEIN and genie_eb_go_gs configurations, neither land temperature, nor standing water on land, exist, but the possibility of different air temperature and land temperature, and of land moisture, are important coupling quantities when other land options are used. The outputs from the atmosphere to the land surface are air temperature (°C) and precipitation rate (m s^{-1}). If the atmospheric chemistry module (atchem) is included, a further input to the atmosphere is CO_2 concentration (ppmv). A further input to the atmosphere is sea-ice temperature (°C). The output from the atmosphere to sea ice is surface air temperature, specific humidity, and shortwave radiation (W m^{-2}).

15 4 Meshes and timesteps

In referring to different meshes, the convention used here and elsewhere is to specify the number of grid cells for longitude first, followed by that for latitude, and then by that for depth levels (when required). Various horizontal meshes have been implemented, but the meshes preferred at present are 36×36 s (with constant increments of sine of latitude and thus equal-area grid cells) and 64×32 (5.625° resolution, with constant and equal increments of latitude and longitude), both with either 8 or 16 depth levels in the ocean (exactly logarithmically-spaced, with a maximum depth of 5000 m). Two further meshes are now available: 72×72 s, with 16 levels; 36×60 ($10^\circ \times 3^\circ$ resolution), with 8 levels. The motivation for these four meshes is according to scientific focus: the 36×36 s mesh affords maximum efficiency and has been used for very large ensembles (e.g., Marsh et al., 2004), multiple biogeochemical simulations (e.g., Cameron et al., 2005; Ridgwell et al., 2007), and very long simulations, of up to 1 Ma,

The “genie_eb_go_gs” configuration of GENIE

R. Marsh et al.

[Title Page](#)

[Abstract](#)

[Introduction](#)

[Conclusions](#)

[References](#)

[Tables](#)

[Figures](#)

◀

▶

◀

▶

[Back](#)

[Close](#)

[Full Screen / Esc](#)

[Printer-friendly Version](#)

[Interactive Discussion](#)



to investigate glacial-interglacial cycles (T. Lenton, personal communication, 2008) and rock weathering and the carbon cycle (G. Colbourn, personal communication, 2008); the 64×32 mesh exactly matches the surface exchange mesh of the alternative 3-D dynamical atmospheric model, an intermediate complexity general circulation model (IGCM), hence eliminating the need for interpolation (which can degrade simulations due to mismatches between land-ocean masks). The 64×32 mesh has higher zonal and polar resolution than 36×36 s but lower meridional resolution in lower latitudes and requires a much shorter timestep; by preserving the 36×36 s land-sea distribution, the 72×72 s ($\times 16$) mesh tests the effect of doubled resolution in all three dimensions; the 36×60 mesh provides the highest resolution in the meridional dimension, to allow improved representation of ocean water mass formation, deep sinking and cryospheric processes, at mid and high latitudes.

Figure 1 shows ocean topography discretized on the four different meshes. Also required, for a given horizontal mesh, is a runoff direction for land gridboxes (north, south, east, west), and these directions are also indicated in Fig. 1. Topography and catchment area representations are combined in files stored in the directory `genie-goldstein/data/input`:

- `worbe2.k1` (36×36 s, 8 levels)
- `igcmv1.k1` (64×32 , 8 levels)
- `g7272s.k1` (72×72 s, 16 levels)
- `g3660l.k1` (36×60 , 8 levels)

The 6-character mesh identifier, <world> (`worbe2`, `igcmv1`, `g7272s` or `g3660l`), is specified in the GENIE configuration file. For each of these mesh files, a further set of files is required: for solution of the barotropic streamfunction; to force the wind-driven ocean circulation (ocean momentum balance); to advect moisture in the atmosphere; for objective evaluation of model error. The protocol for these filenames, and the source of

The “`genie_eb_gs`” configuration of GENIE

R. Marsh et al.

[Title Page](#)

[Abstract](#)

[Introduction](#)

[Conclusions](#)

[References](#)

[Tables](#)

[Figures](#)

◀

▶

◀

▶

[Back](#)

[Close](#)

[Full Screen / Esc](#)

[Printer-friendly Version](#)

[Interactive Discussion](#)



data, are provided in Table 1. Experimentation is in progress with further alternative meshes, e.g., 64×64 (5.625° longitude $\times 2.8125^\circ$ latitude), and up to 32 depth levels. Once successfully tested, such meshes will be added to the GENIE framework.

In principle, any arbitrarily-varying resolution with latitude can be specified. However, horizontal resolutions higher than around 72×72 are liable to lead to degradation of efficiency owing to numerical boundary instabilities requiring an implicit scheme for efficient solution (Edwards and Shepherd, 2001). At sufficiently high resolution, an instability related to baroclinic eddy formation is likely to occur, although the model does not include sufficient physics to represent eddies correctly. With 32 vertical levels, explicit timestepping in the vertical becomes inefficient, as found by Müller et al. (2006) who use an implicit scheme in the vertical that is not yet implemented in the GENIE version. In practice the EMBM and sea ice normally share the same horizontal resolution as the GOLDSTEIN ocean. Although GENIE also allows for the coupling of modules with different horizontal resolution, in the case of the `genie_eb_gs` configuration this would lead to unnecessary interpolation with associated errors and degradation in performance.

According to the horizontal mesh in use, maximum timesteps are recommended as follows:

- GOLDSTEIN and Sea Ice Timestep: 100 year^{-1} ($36 \times 36 \text{ s}$); 200 year^{-1} (64×32 , 36×60 , $72 \times 72 \text{ s}$)
- EMBM Timestep: asynchronous with default of 5 atmospheric timesteps per ocean timestep (i.e., 500 year^{-1} or 1000 year^{-1} , depending on the horizontal resolution)

The timestep frequencies (ocean timesteps per year, atmospheric timesteps per ocean timestep) are specified in the GENIE configuration file. Further essential changes when using the higher resolution 64×32 , 36×60 and $72 \times 72 \text{ s}$ meshes, to ensure numerical stability, are as follows:

- Increase sea-ice diffusivity to a recommended value of $20\,000 \text{ m}^2 \text{ s}^{-1}$
- With such high diffusivity, it is necessary to switch from explicit to implicit sea ice timestepping, i.e., compile with the “dimpsic” option in “genie_seaice/src/fortran/makefile”

- 5 One further essential change is necessary when using the 64×32 and 36×60 meshes:
- Decrease the slope of the meridional heat diffusivity function to 0.0

One further change is necessary when using the 36×60 mesh, as Greenland is detached from North America (it is attached in the other three meshes):

- Specify `isles=2` in `genie-goldstein/src/fortran/ocean.cmn` (by default, `isles=1`), and compile with the “`disles`” option in `genie-goldstein/src/fortran`

10

5 Constants, parameters and prescribed inputs

Key constants in `genie_eb_go_gs` are listed in Tables 2–5 (global, ocean, atmosphere and sea ice, respectively). Default values for the key parameters of the components described here are listed in Table 6, and are declared in `genie-main/runtime_defaults.sh`.

15 Some parameter values are altered according to model configuration (see Sect. 4). The 12 key parameters in Table 6 are commonly used in model tuning. Optimally-tuned parameter values have been obtained by Hargreaves et al. (2004), Beltran et al. (2006) and Price et al. (2006), using a variety of methods. The latter study reports the results of all three tuning exercises. Note that these tuned values apply specifically
20 to the $36 \times 36s$ ($\times 8$) resolution and are not likely to be optimal for other resolutions. Here we use non-tuned default values.

In addition to these key parameters, the EMBM also requires several prescribed inputs: the wind field (m s^{-1}), from annual-mean or monthly-mean NCEP/NCAR reanalysis, interpolated onto the model grid (10-m winds are used, although they represent

The “`genie_eb_go_gs`” configuration of GENIE

R. Marsh et al.

[Title Page](#)

[Abstract](#)

[Introduction](#)

[Conclusions](#)

[References](#)

[Tables](#)

[Figures](#)

◀

▶

◀

▶

[Back](#)

[Close](#)

[Full Screen / Esc](#)

[Printer-friendly Version](#)

[Interactive Discussion](#)



vertically averaged advection); and a climatological albedo, as a function of latitude. The ocean module also requires wind stresses (from Josey et al., 1998). Figure 2 shows the annual-mean winds (direction and speed) on the four default meshes. Figure 3 shows corresponding meridional profiles of climatological albedo (Fig. 3a) and the heat diffusivity for the default parameter values (Fig. 3b). The meridional profile of heat diffusivity in the atmosphere is controlled by three separate parameters (see Table 6).

6 Control run climatologies

The runtime nomenclature for the basic GENIE-1 climate model, compiled by the standard procedure, is `genie_eb_go_gs` (denoting the EMBM atmosphere, GOLDSTEIN ocean and GOLDSTEIN sea-ice modules). Configuration filenames for individual experiments are listed in Table 7. Filenames are prefixed with the experiment name “`spn`” by default. In the following simulations, `genie_eb_go_gs` has been integrated from an initially uniform state for 4000 years. The default version of `genie_eb_go_gs` includes the seasonal cycle of insolation but constant wind forcing. To illustrate spin-up, we show selected annually-averaged integral measures of model climate, using all four meshes (Figs. 4–7). After a few hundred years, the radiation balance and the atmospheric hydrological cycle are largely equilibrated, as evident in the rapid equilibration of global-mean air temperature and specific humidity (output in files `spn.airt` and `spn.q`, see Fig. 4). After around 1000 years, the ocean heat and freshwater content are close to equilibrium, as shown by the evolution of global-mean ocean temperature and salinity (`spn.t` and `spn.s`, see Figs. 5, 6). After 4000 years, the global ocean circulation is very close to equilibrium, as illustrated by the long-term trends in maxima and minima of Atlantic and Pacific overturning rates (`spn.opsit`, see Fig. 7). Broadly speaking, equilibration is similar across the four meshes, with no systematic differences that can be ascribed to grid resolution. We henceforth consider the equilibrium state of the atmosphere, ocean and sea ice at the end of each spin-up (Sects. 6.1–6.6), finishing with

The “`genie_eb_go_gs` configuration of GENIE

R. Marsh et al.

[Title Page](#)

[Abstract](#)

[Introduction](#)

[Conclusions](#)

[References](#)

[Tables](#)

[Figures](#)

◀

▶

◀

▶

[Back](#)

[Close](#)

[Full Screen / Esc](#)

[Printer-friendly Version](#)

[Interactive Discussion](#)



brief model-observation comparisons (Sect. 6.7). Subsequent maps and sections are plotted using netCDF model output (ASCII-format output is also available, for compatibility with the most general range of plotting programs).

6.1 Atmosphere

- 5 Figures 8 and 9 shows the annual-mean air temperature (Fig. 8) and specific humidity (Fig. 9), on the four meshes. The air temperature fields are generally smoother than the specific humidity fields. As noted by EM05, the rapid relaxation of specific humidity means that the field is largely a diagnostic of the underlying surface temperature, while the transport and source terms modify the pattern in a way consistent with the (un-
10 represented) effects of local convection. While evaluation of these (and subsequent) 36×36 s model data against observations has been considered extensively elsewhere (Hargreaves et al., 2004; EM05), we note that agreements are generally good on all four meshes.

6.2 Ocean

- 15 Figures 10–12 show the annual-mean sea surface temperature (Fig. 10), salinity (Fig. 11) and density (Fig. 12). For selected longitudes in the Atlantic and Pacific sectors, we also show temperature and salinity in meridional section (Figs. 13–16). Several features are clear from these maps and sections. Deep and bottom temperature and salinity are influenced by the inter-hemispheric overturning circulation, in
20 particular the export of North Atlantic Deep Water (NADW). At the low horizontal and vertical resolutions used here, Antarctic Bottom Water (AABW) is poorly represented, allowing NADW to unrealistically dominate the abyssal Atlantic Ocean. Considerable improvement in the representation of AABW has recently been achieved by including the effects of a full non-linear equation of state, although extensive model testing is still
25 underway (K. Oliver, personal communication, 2008).

The average convection depth level over the entire 4000-year spin-up is shown in

The “genie_eb_gs” configuration of GENIE

R. Marsh et al.

[Title Page](#)

[Abstract](#)

[Introduction](#)

[Conclusions](#)

[References](#)

[Tables](#)

[Figures](#)

◀

▶

◀

▶

[Back](#)

[Close](#)

[Full Screen / Esc](#)

[Printer-friendly Version](#)

[Interactive Discussion](#)



The “genie_eb_go_gs” configuration of GENIE

R. Marsh et al.

[Title Page](#)

[Abstract](#)

[Introduction](#)

[Conclusions](#)

[References](#)

[Tables](#)

[Figures](#)

◀

▶

◀

▶

[Back](#)

[Close](#)

[Full Screen / Esc](#)

[Printer-friendly Version](#)

[Interactive Discussion](#)



Fig. 17 (note that the panels show depth level indices rather than actual depths). This information is obtained from the file goldstein/spn.cost, which records the total number of levels mixed during a simulation. An average convection depth level at each ocean gridpoint is therefore obtained as the integrated number of mixed levels divided by the number of ocean timesteps in the spin-up (4000×100 , or 4000×200). Figure 17 illustrates localized centres of deep convection in the North Atlantic and around Antarctica: >3 levels convected on the 3636 s, 6432 and 3660 meshes; >6 levels convected on the 7272 s mesh (due to doubled vertical resolution).

6.3 Sea ice

- 10 Figures 18 and 19 show the annual-mean sea ice thickness (Fig. 18) and concentration (Fig. 19). Where annual-mean sea ice concentration exceeds 0.885, concentration is in fact very close to 1.0 all year round, with a very small residual fraction representing leads. Gridboxes where annual-mean concentration is non-zero but less than 0.885 experience seasonal sea ice cover. The extent of seasonality (in months of ice-cover) can be estimated by multiplying annual-mean concentration by 12. Thickest and most
- 15 perennial sea ice develops in the Arctic, in reasonable agreement with observations. Arctic sea ice is substantially thickest with the 36×60 mesh. The extent and thickness of Southern Ocean sea ice varies considerably with choice of mesh. The most extensive, strongly seasonal, distribution of sea ice is obtained with the 72×72 s mesh, while the
- 20 most limited distribution is obtained with the 36×36 s mesh. The reasons for these differences are probably not directly related to inadequate spatial resolution, but rather due to feedbacks involving the atmosphere and the ocean.

6.4 Vertical and internal fluxes of heat and moisture

- 25 Figures 20–31 show annual-mean vertical and internal components of heat and freshwater flux, for both atmosphere and ocean. Annual means shown here are averaged for the 500-year period from year 3501 to year 4000. In Figs. 20–23, the shortwave

flux into the atmosphere (top left panels) is clearly demarcated by the land-sea boundary, with stronger fluxes over land. This is a consequence of zero heat absorption by land in the absence of a more sophisticated land scheme (the heat capacity of land is neglected). Consequently the atmosphere absorbs all incident shortwave radiation over land, while the atmosphere absorbs 30% of shortwave radiation over the ocean (specified by the parameter detailed in Table 4). The longwave heat flux into the atmosphere (top right panels in Figs. 20–23) is negative everywhere, reaching minima where specific humidity is lowest. The sensible heat flux into the atmosphere (middle left panels) is strongest where the ocean is strongly cooled through import of relatively warm water to deep sinking sites, notably the North Atlantic subpolar gyre. The latent heat flux into the atmosphere (middle right panels) is strongly correlated with precipitation and the associated strong condensation of water vapour (see below). The highest fluxes are located in the tropics, but secondary maxima coincide with mid-latitude storm tracks, coincident with strong evaporation in the vicinity of warm ocean currents. Combined together, these four components yield a familiar climatological pattern of net heat flux into the atmosphere (lower left panels), with heat gain (loss) in low (high) latitudes that must be balanced by meridional heat transports in the atmosphere and ocean (see Sect. 6.5 below).

In Figs. 24–27, the shortwave heat flux into the ocean (top left panels) is a constant 70% of incident shortwave radiation (30% being absorbed in the overlying atmosphere), although levels are reduced somewhat at high latitudes due to a higher albedo associated with sea ice formation. The longwave heat flux into the ocean is a relatively small term in the heat balance, associated with the downwelling part of re-radiated longwave flux. The sensible heat flux into the ocean, negative everywhere, is identical and opposite to the counterpart flux into the atmosphere. The latent heat flux into the ocean, again negative everywhere, mirrors the pattern of evaporation (see below). Combined together, these four components yield patterns of net heat flux into the ocean (lower left panels) at low latitudes, with strong localized heat loss over western boundary currents and at sites of high latitude convection (see Fig. 17).

The “genie_eb_go_gs” configuration of GENIE

R. Marsh et al.

[Title Page](#)

[Abstract](#)

[Introduction](#)

[Conclusions](#)

[References](#)

[Tables](#)

[Figures](#)

◀

▶

◀

▶

[Back](#)

[Close](#)

[Full Screen / Esc](#)

[Printer-friendly Version](#)

[Interactive Discussion](#)



In Figs. 28–31, evaporation is equivalently a negative freshwater flux into the ocean (top left panels), with maxima over the subtropical gyres. Precipitation (top right panels) to an extent coincides with strong evaporation. The precipitation located over the continents does not appear in the field that directly forces ocean surface salinity (shown here), but reaches the ocean as runoff (middle left panels). The consequence of seasonal freezing and melting of sea ice is a net freshwater flux that effectively removes freshwater in regions of sea ice formation and adds freshwater in regions of sea ice melt (middle right panels), with strongest (weakest) signatures on the 36×60 (36×36 s) mesh. Combined together (lower left panels), these four components yield net freshwater flux gain at low and middle latitudes, with net freshwater loss in the subtropics (strongest towards eastern boundaries) and at highest latitudes. Strongest net freshwater gain is associated with major rivers.

6.5 Meridional heat transports

Figure 32 shows oceanic, atmospheric and total meridional heat transports on the four meshes. The data plotted here are written in ASCII format to goldstein/spn.fofy (oceanic transports) and embm/spn.fofy (atmospheric transports), and correspond to an instantaneous (1 January) climate state. As estimated from observations (Trenberth and Caron, 2001), atmospheric heat transport is dominant at most latitudes. Of the four meshes, the 64×32 mesh supports strongest northward heat transport, largely due to a stronger oceanic Conveyor (northward heat transport throughout the Atlantic sector – not shown), while the 36×60 mesh supports the strongest southward heat transport in the Southern Hemisphere (again largely attributed to ocean heat transport in the Southern Ocean). Transports are in general highly consistent with available data (e.g., Trenberth and Caron, 2001) and results obtained with more complex models (e.g., IPCC, 2007c).

The “genie_eb_gs_gs” configuration of GENIE

R. Marsh et al.

[Title Page](#)

[Abstract](#)

[Introduction](#)

[Conclusions](#)

[References](#)

[Tables](#)

[Figures](#)

◀

▶

◀

▶

[Back](#)

[Close](#)

[Full Screen / Esc](#)

[Printer-friendly Version](#)

[Interactive Discussion](#)



6.6 Ocean circulation

Figure 33 shows the barotropic streamfunction on each mesh. These data are written in ASCII format to goldstein/spn.opsi. For each of the four meshes, barotropic transports are somewhat weak compared to both observations and more complex models. This is a consequence of the non-viscous representation of frictional effects in GOLDSTEIN (see Killworth, 2003). There are also substantial differences between the meshes. The most notable difference is in the Southern Ocean, where circumpolar transport ranges from ~ 30 Sv (36×36 s, 64×32), through ~ 40 Sv (72×72 s) to ~ 50 Sv (36×60). These differences appear to be linked to the number of gridcells across Drake Passage – with fewer gridcells (as in 36×36 s and 64×32 meshes), the frictional influence of adjacent coasts is stronger and this weakens transport.

Figures 34–36 show annual-mean meridional overturning streamfunctions (global, and Atlantic and Pacific separately) on each mesh. These data are written in ASCII format to goldstein/spn.opav, goldstein/spn.opava, and goldstein/spn.opavp. Again the most striking difference between the meridional overturning on the four meshes is in the Southern Ocean. In contrast to the other three meshes, a strong counter-clockwise cell is evident on the 36×60 mesh (Fig. 34). This is supported by deep sinking of ~ 15 Sv south of $\sim 60^\circ$ S, consistent with the corresponding convection pattern in Fig. 17. On each mesh, the Atlantic overturning circulation is in a strong “Conveyor” mode (Fig. 35), although this is ensured through the specification of an explicit additional Atlantic-Pacific moisture flux (default value 0.32 Sv – see Table 6). We note that the Atlantic overturning is strongest on the 64×32 mesh and weakest on the 72×72 s mesh. Only on the 64×32 and 36×60 meshes does Atlantic overturning extend perceptibly into the Nordic Seas (beyond $\sim 60^\circ$ N). The Pacific is characterized by a counter-clockwise cell, comprising the northward import and upwelling of deep water (Fig. 36). This cell is clearly strongest on the 36×60 mesh, commensurate with the strongest sinking at southern high latitudes (Fig. 34). It is known from tuning exercises with several of these mesh configurations (R. Myerscough, in preparation, 2009) that the

The “genie_eb_go_gs” configuration of GENIE

R. Marsh et al.

[Title Page](#)

[Abstract](#)

[Introduction](#)

[Conclusions](#)

[References](#)

[Tables](#)

[Figures](#)

◀

▶

◀

▶

[Back](#)

[Close](#)

[Full Screen / Esc](#)

[Printer-friendly Version](#)

[Interactive Discussion](#)



structure and strength of the overturning circulation are particularly sensitive to some of the key parameter values: the results given here are for untuned default parameters and should therefore be regarded only as illustrative.

6.7 Model-observation comparisons

- 5 For basic model evaluation, selected annual-mean observations are re-gridded on each mesh, and to each depth level in the ocean. Atmospheric observations of surface air temperature and specific humidity are from the NCEP/NCAR reanalysis. Ocean observations of potential temperature and salinity are from the Levitus et al. (1998) climatology. Model-observation differences, or errors, are combined for the atmosphere
10 and the ocean separately. Composite errors are obtained, with weighting to account for both variable grid-cell areas (64×32 and 36×60 meshes) and for differences in the observed variance of the two fields. In the case of the 36×36 s mesh the mean error corresponds to that calculated in EM05. These error diagnostics are calculated as a standard procedure in GENIE experiments. Table 8 lists weighted model-observation
15 root mean square errors, for the atmosphere and ocean, and for each mesh, where the model data are annual-mean values for the last 500 years of each spin-up experiment. Comparison of error measures between different grids depends on essentially subjective choices of error weighting, however we note that with our choices the smallest (largest) atmospheric error is obtained with the 36×60 (36×36 s) mesh, while the
20 smallest (largest) ocean error is obtained with the 72×72 s (64×32) mesh. These errors are presented here to illustrate how different versions of GENIE may be co-evaluated. Given the historical developmental focus on the 36×36 s mesh, and since no attempt has been made here to tune key parameters for each mesh, the four meshes cannot
25 be adequately evaluated on the basis of the errors in Table 8. This caveat is further addressed below.

For a more detailed example of co-evaluation of the four meshes, Fig. 37 shows annual-mean “model minus observation” differences for zonal-averages of air temperature, specific humidity, sea surface temperature and sea surface salinity. General

The “genie_eb_gs” configuration of GENIE

R. Marsh et al.

[Title Page](#)

[Abstract](#)

[Introduction](#)

[Conclusions](#)

[References](#)

[Tables](#)

[Figures](#)

◀

▶

◀

▶

[Back](#)

[Close](#)

[Full Screen / Esc](#)

[Printer-friendly Version](#)

[Interactive Discussion](#)



aspects of this basic model-observation comparison are summarized as follows:

- Air temperature: generally lower than observed in the Northern Hemisphere, most severely with the 36×60 mesh; both lower and higher than observed in the Southern Hemisphere, the results for the 64×32 mesh being too warm, while those for the 72×72 s mesh are too cold
- Specific Humidity: generally higher than observed, most strikingly with the 36×36 s mesh; smaller overall differences are obtained with the 36×60 and 72×72 s meshes; notably lower than observed in the northern extra-tropics, while differences over the Southern Ocean are most positive with the 64×32 mesh
- Sea Surface Temperature: generally higher than observed, except in the high-latitude Northern Hemisphere; largest Southern Hemisphere positive differences with the 64×32 mesh; smallest overall differences with the 36×60 mesh; largest overall positive differences with the 36×36 s mesh
- Sea Surface Salinity: generally similar differences south of northern mid-latitudes, with slightly positive differences in the Southern Ocean and northern mid-latitudes, slightly negative differences in the tropics and subtropics; stronger positive (negative) differences at northern high latitudes with the 64×32 (36×60) mesh

The closer agreement with some observations using the 36×36 s mesh, notably air temperature, may be due to a better ad hoc choice of parameters at that resolution. In the original model development (C-GOLDSTEIN, and early versions of *genie_eb_gs*), we exclusively used the 36×36 s mesh, and although the parameters used here are default values, these were subjectively chosen to obtain good model-observation agreement on this “original” mesh. Some of the larger model-observation differences arising with the other three meshes may be attributed to our choice of common default values for the key parameters (with the aforementioned exceptions of sea-ice diffusivity and the slope of the meridional heat diffusivity function).

The “*genie_eb_gs*” configuration of GENIE

R. Marsh et al.

[Title Page](#)

[Abstract](#)

[Introduction](#)

[Conclusions](#)

[References](#)

[Tables](#)

[Figures](#)

[◀](#)

[▶](#)

[◀](#)

[▶](#)

[Back](#)

[Close](#)

[Full Screen / Esc](#)

[Printer-friendly Version](#)

[Interactive Discussion](#)



Some notable model-observation differences are clearly associated with the thickness and seasonality of sea ice (Figs. 18, 19): thickest Arctic sea ice and the coldest Northern Hemisphere with the 36×60 mesh; minimal sea ice around Antarctica and the warmest Southern Ocean with the 64×32 mesh. Large salinity differences in the high-latitude Northern Hemisphere appear to be associated with subtle differences in the surface freshwater balance (Figs. 28–31): with the 64×32 mesh, the large fresh anomaly centred on 70° N is associated with high runoff to the Arctic; with the 36×60 mesh, the large saline anomaly in the Arctic is associated with extensive and strong brine rejection, due to gradual long-term thickening of Arctic sea ice in that spin-up (Fig. 30). In conclusion, the influence of resolution clearly varies by region. This issue is revisited in the Discussion section.

7 Standard climate experiments

As examples of experiments with `genie_eb_go_gs`, we choose the CMIP protocols for CO₂ and freshwater forcing (see http://www-pcmdi.llnl.gov/projects/cmip/coord_expt.php), followed by classic AMOC hysteresis experiments (e.g., Rahmstorf et al., 2005).

7.1 Equilibrium climate sensitivity and transient climate response

In the equilibrium climate sensitivity experiments, the model is spun up to equilibrium under doubled pre-industrial CO₂ concentration of 556 ppmv. Transient climate response experiments are restarted from the end of the original spin-up (under pre-industrial CO₂), increasing CO₂ at 1% per annum, compounded. After 70 years, the CO₂ concentration approximately doubles to 560 ppmv. Figures 38 and 39 show maps of the change of annual-mean air temperature due to CO₂ doubling, at the end of each equilibrium experiment (Fig. 38), and in the 70th year of each transient experiment (Fig. 39). In the equilibrium experiments, warming exceeds 2°C everywhere, and exceeds 3°C at high latitudes, on all four meshes. There are some notable differences

The “`genie_eb_go_gs`” configuration of GENIE

R. Marsh et al.

[Title Page](#)

[Abstract](#)

[Introduction](#)

[Conclusions](#)

[References](#)

[Tables](#)

[Figures](#)

◀

▶

◀

▶

[Back](#)

[Close](#)

[Full Screen / Esc](#)

[Printer-friendly Version](#)

[Interactive Discussion](#)



between the meshes, mainly attributed to differences in initial sea-ice thickness and distribution. In particular, sea ice around Antarctica varies considerably between the meshes (see Fig. 16), and this leads to a wide variation in the regional response of air temperature to increased CO₂. The strongest warming is coincident with the melt back of this sea ice, exceeding 5°C on the 36×36 s and 36×60 meshes. The formal definition of climate sensitivity, the change of global-mean air temperature with doubled CO₂, is nevertheless similar for each mesh, lying in the range 2.85–3.13°C (see Table 9).

Global-mean temperature increases at CO₂ doubling in the transient experiments are reduced to about two thirds of those in the equilibrium response (see Table 9), and the patterns of warming are also somewhat different. In particular, sea ice melting is only partial, with modest Arctic warming but no discernible additional warming around Antarctica. The transient climate response, expressed as global-mean temperature increase, varies somewhat more between meshes compared to equilibrium climate sensitivity, from 1.67°C (36×60 mesh) to 1.97°C (72×72 s mesh). In summary here, the magnitude (climate sensitivities) and spatial patterns of these responses are consistent with the results obtained with more complex models (IPCC, 2007a), although we note that climate sensitivity in *genie_eb_go_gs* is largely controlled by the choice of radiative forcing sensitivity to doubled CO₂ (see Table 4).

7.2 Freshwater hosing

Freshwater hosing experiments are continued from the end of the original spin-up experiments. An additional component is added to the surface freshwater flux in the Atlantic zone 50–70° N, equally distributed across all gridcells. Figure 40 shows AMOC intensity during freshwater hosing, with a constant additional freshwater flux applied for 100 years, at 0.1 Sv (Fig. 40a) and 1.0 Sv (Fig. 40b). For three of the meshes (36×36 s, 64×32, 36×60), the Atlantic overturning weakens by 10–20% under 0.1 Sv forcing, and subsequently recovers within decades once the forcing ceases. On the 72×72 s mesh, the overturning collapses under 0.1 Sv forcing, and only slowly starts to recover. By contrast, the overturning collapses on all four meshes under 1.0 Sv forcing, and re-

The “*genie_eb_go_gs*” configuration of GENIE

R. Marsh et al.

[Title Page](#)

[Abstract](#)

[Introduction](#)

[Conclusions](#)

[References](#)

[Tables](#)

[Figures](#)

◀

▶

◀

▶

[Back](#)

[Close](#)

[Full Screen / Esc](#)

[Printer-friendly Version](#)

[Interactive Discussion](#)



mains collapsed for at least 100 years after forcing ceases. The AMOC responses to freshwater hosing shown here are broadly consistent with responses obtained with a wide range of climate models (Stouffer et al., 2006).

7.3 AMOC hysteresis

- 5 Hysteresis experiments are continued from the end of the original spin-up experiments. An additional freshwater flux is applied as in the hosing experiments. Figure 41 shows AMOC hysteresis loops, created by first increasing and then decreasing this freshwater flux at 0.05 Sv per 1000 years, for the four meshes. Hysteresis is evident with each mesh, with collapsed overturning not recovering until the freshwater flux decreases well
10 below the value at which collapse took place as the flux was first increased. However, initial state stability varies considerably. The initial state (at zero freshwater flux) for each mesh is summarized as follows:
- 15 – just monostable for the 36×36 s mesh
– strongly bistable for the 64×32 mesh
– most strongly monostable for the 36×60 mesh
– marginally bistable for the 72×72 s mesh

The differences between 36×36 s, 64×32 and 72×72 s meshes are broadly consistent with findings of Lenton et al. (2007), in which an intermediate-complexity general circulation model of the atmosphere (IGCM) was used in place of the EMBM, and stability
20 was inferred from a series of equilibrium experiments with GENIE-2. Key determinants of stability are oceanic transports and surface fluxes of freshwater, which are extensively analysed and discussed in Lenton et al. (2007).

The “genie_eb_gos” configuration of GENIE

R. Marsh et al.

[Title Page](#)

[Abstract](#)

[Introduction](#)

[Conclusions](#)

[References](#)

[Tables](#)

[Figures](#)

◀

▶

◀

▶

[Back](#)

[Close](#)

[Full Screen / Esc](#)

[Printer-friendly Version](#)

[Interactive Discussion](#)



8 Summary and discussion

We have described the basic GENIE-1 climate model: specifically `genie_eg_go_gs`. A limited range of the available options is presented to illustrate the nature and use of the model, namely the choice of four different meshes, and a small range of standard climate experiments to address the sensitivity of climate and ocean circulation to external forcing. While the resulting models show generally similar climate and ocean states, it is clear that the choice of mesh, and corresponding resolution, has a significant effect on some of the results. While this grid dependence complicates interpretation, there is no reason to suppose that it is peculiar to GENIE.

We find that grid resolution influences model behaviour both globally and regionally, and of course also affects computational efficiency. For example, the computational cost of a given length integration using the 36×36 s mesh is an order of magnitude less than with the 64×32 mesh, even though resolution in latitude is actually higher close to the equator. There are corresponding implications for atmospheric and oceanic transports in this region, where the structure of ocean currents and prescribed atmospheric winds is complex. However, the advantage of better meridional resolution towards the poles, with the 64×32 and 36×60 meshes, is that geostrophic circumpolar flow in the Arctic can be represented. This would also be possible in principle at 72×72 s resolution, but not using the 36×36 s mesh.

It could be argued that, because no more physics is included, little advantage is gained with meshes that are considerably more costly in computational terms. The 64×32 and 36×60 meshes accommodate many more grid-points in the Arctic, but connectivity of the Arctic and North Atlantic remains limited, with the majority of deep sinking located at around 60° N. However, previous studies (Lenton et al., 2007) and the present inter-comparison suggest that substantially less additional (implicit) Atlantic-Pacific moisture flux is required to ensure a Conveyor mode THC in the case of the 64×32 mesh. We also re-emphasized here our decision to use default parameters throughout (except in a few specific instances), and we posulate that the alternative

GMDD

2, 1–79, 2009

The “`genie_eb_go_gs` configuration of GENIE

R. Marsh et al.

[Title Page](#)

[Abstract](#)

[Introduction](#)

[Conclusions](#)

[References](#)

[Tables](#)

[Figures](#)

◀

▶

◀

▶

[Back](#)

[Close](#)

[Full Screen / Esc](#)

[Printer-friendly Version](#)

[Interactive Discussion](#)



meshes may produce more realistic results (than the 36×36 s mesh) if key parameters are re-tuned as in earlier studies (Hargreaves et al., 2004; Beltran et al., 2006, Price et al., 2006).

A “unique selling point” of GENIE is the combination of flexibility and computational efficiency. Swapping the EMBM for an atmospheric general circulation model of intermediate complexity (comprising `genie_ig_go_sl`, or GENIE-2), it is possible to comprehensively evaluate the stability of the thermohaline circulation through both equilibrium experiments (Lenton et al., 2007), and “classic” hysteresis experiments (Lenton et al., 2008), yet neither study is yet feasible with even coarse-resolution climate models of fuller complexity (as featured in IPCC, 2007c). However, even these GENIE-2 experiments are highly ambitious in both ensemble size (totalling around half a million years of simulation, for Lenton et al., 2007) and duration (nearly 1 month of continuous computing, for Lenton et al., 2008). The advantage of `genie_eb_go_gs`, and associated GENIE-1 configurations, remains the speed of computation – by comparison with GENIE-2, simulations are around two orders of magnitude faster.

Future short papers will report a series of updates on the present results, as progress continues in several areas: parameter tuning; methodologies for palaeoclimate experiments; further developments of GENIE-1 components that lead to improvements on the results reported here.

20 Acknowledgements. The GENIE (NER/T/S/2002/00217) and ongoing GENIEfy (NE/C515904) projects were funded by the UK Natural Environment Research Council (NERC). The development of alternative ocean meshes was in part funded by the NERC Rapid Climate Change project “The role of the cryosphere on modulating the THC of the North Atlantic” (Ref. NER/T/S/2002/00462). R. J. Myerscough is a GENIEfy e-Science PhD student. The GENIE framework was originally developed by Gethin Williams and Dan Lunt at the University of Bristol. Paul Valdes (University of Bristol) and Tim Lenton (University of East Anglia) led the GENIE and GENIEfy projects, respectively.

The “`genie_eb_go_gs`” configuration of GENIE

R. Marsh et al.

[Title Page](#)

[Abstract](#)

[Introduction](#)

[Conclusions](#)

[References](#)

[Tables](#)

[Figures](#)

◀

▶

◀

▶

[Back](#)

[Close](#)

[Full Screen / Esc](#)

[Printer-friendly Version](#)

[Interactive Discussion](#)



References

GMDD

2, 1–79, 2009

- Beltran, C., Edwards, N. R., Haurie, A., Vial, J.-P., and Zachary, D. S.: Oracle-Based Optimization Applied to Climate Model Calibration, *Environmental Modelling and Assessment*, 11, 31–43, 2006.
- 5 Cameron, D. R., Lenton, T. M., Ridgwell, A. J., Shepherd, J. G., Marsh, R. and Yool, A.: A factorial analysis of the marine carbon cycle controls on atmospheric CO₂, *Glob. Biogeochem. Cy.*, 19(4), 1–12, 2005.
- Claussen, M., Mysak, L. A., Weaver, A. J., et al.: Earth system models of intermediate complexity: closing the gap in the spectrum of climate system models, *Clim. Dynam.*, 18, 579–586, 10 2002.
- Edwards, N. R., Willmott, A. J., and Killworth, P. D.: On the role of topography and wind stress on the stability of the thermohaline circulation, *J. Phys. Oceanogr.*, 28, 756–778, 1998.
- Edwards, N. R. and Shepherd, J. G.: Multiple thermohaline states due to variable diffusivity in a hierarchy of simple models, *Ocean Modelling*, 3, 67–94, 2001.
- 15 Edwards, N. R. and Shepherd, J. G.: Bifurcations of the thermohaline circulation in a simplified three-dimensional model of the world ocean and the effects of interbasin connectivity, *Clim. Dynam.* 19, 31–42, 2002.
- Edwards, N. R. and Marsh, R.: Uncertainties due to transport-parameter sensitivity in an efficient 3-D ocean-climate model, *Clim. Dynam.*, 24, 415–433, 2005.
- 20 Fiadeiro, M. E. and Veronis, G.: Weighted-mean schemes for finite-difference approximation to advection-diffusion equation, *Tellus*, 29(6), 512–522, 1977.
- Hargreaves, J. C., Annan, J. D., Edwards, N. R. and Marsh, R.: An efficient climate forecasting method using an intermediate complexity Earth System Model and the ensemble Kalman filter, *Clim. Dynam.*, 23, 745–760, 2004.
- 25 IPCC: WG1 AR4 Report, Chapter 10, “Global Climate Projections”, 2007a.
- IPCC: WG1 AR4 Report, Chapter 6, “Palaeoclimate”, 2007b.
- IPCC: WG1 AR4 Report, Chapter 8, “Climate Models and their Evaluation”, 2007c.
- 30 Josey, S. A., Kent, E. C., and Taylor, P. K.: The Southampton Oceanography Centre (SOC) Ocean-Atmosphere Heat, Momentum and Freshwater Flux Atlas. Southampton Oceanography Centre Rep. 6, Southampton, United Kingdom, 30 pp. and figures, 1998.
- Killworth, P. D.: Some physical and numerical details of frictional geostrophic models, Southampton Oceanography Centre Internal Report, No. 90, 2003.

The “genie_eb_gos” configuration of GENIE

R. Marsh et al.

[Title Page](#)

[Abstract](#)

[Introduction](#)

[Conclusions](#)

[References](#)

[Tables](#)

[Figures](#)



[Back](#)

[Close](#)

[Full Screen / Esc](#)

[Printer-friendly Version](#)

[Interactive Discussion](#)



The “genie_eb_gs” configuration of GENIE

R. Marsh et al.

[Title Page](#)

[Abstract](#)

[Introduction](#)

[Conclusions](#)

[References](#)

[Tables](#)

[Figures](#)

◀

▶

◀

▶

[Back](#)

[Close](#)

[Full Screen / Esc](#)

[Printer-friendly Version](#)

[Interactive Discussion](#)



Lenton, T. M., Marsh, R., Price, A. R., Lunt, D. J., Aksenov, Y., Annan, J. D., Cooper-Chadwick, T., Cox, S. J., Edwards, N. R., Goswami, S., Hargreaves, J. C., Harris, P. P., Jiao, Z., Livina, V. N., Payne, A. J., Rutt, I. C., Shepherd, J. G., Valdes, P. J., Williams, G., Williamson, M. S., and Yool, A.: Effects of atmospheric dynamics and ocean resolution on bi-stability of the thermohaline circulation examined using the Grid ENabled Integrated Earth system modelling (GENIE) framework, *Clim. Dynam.*, 29(6), 591–613, doi:10.1007/s00382-007-0254-9, 2007.

Lenton, T. M., Myerscough, R. J., Marsh, R., Livina, V. N., Price, A. R., Cox, S. J., and the GENIE team: Using GENIE to study a tipping point in the climate system, *Philosophical Transactions of the Royal Society A*, doi:10.1098/rsta.2008.0171, in press, 2008.

Levitus, S., Boyer, T. P., Conkright, M. E., OrsquoBrien, T., Antonov, J., Stephens, C., Stathopoulos, L., Johnson, D., and Gelfeld, R.: NOAA Atlas NESDIS 18, World Ocean database 1998, Vol. 1, Introduction, US Government Printing Washington DC, 346 pp., 1998.

Marsh, R., Yool, A., Lenton, T. M., Gulamali, M. Y., Edwards, N. R., Shepherd, J. G., Krznaric, M., Newhouse, S., and Cox, S. J.: Bistability of the thermohaline circulation identified through comprehensive 2-parameter sweeps of an efficient climate model, *Clim. Dynam.*, 23(7–8), 761–777, doi:10.1007/s00382-004-0474-1, 2004.

Millero, F. J.: Annex 6, freezing point of seawater. *Unesco Tech.Papers in the Marine Sciences*, 28, 29–35, 1978.

Müller, S. A., Joos, F., Edwards, N. R., and Stocker, T. F.: Water mass distribution and ventilation time scales in a cost-efficient, 3-dimensional ocean model, *J. Climate*, 19, 5479–5499, 2006.

Myerscough, R. J.: Thermohaline circulation stability in climate models of varying resolution and complexity, PhD thesis, University of Southampton, in preparation, 2009.

Plattner, G.-K., Knutti, R., Joos, F., Stocker, T. F., von Bloh, W., Brovkin, V., Cameron, D., Driesschaert, E., Dutkiewicz, S., Eby, M., Edwards, N. R., Fichefet, T., Hargreaves, J. C., Jones, C. D., Loutre, M. F., Matthews, H. D., Mouchet, A., Müller, S. A., Nawrath, S., Price, A., Sokolov, A., Strassmann, K. M., and Weaver, A. J.: Long-term climate commitments projected with climate – carbon cycle models, *J. Climate*, 21, 2721–2751, 2008.

Price, A. R., Voutchkov, I. I., Pound, G. E., Edwards, N. R., Lenton, T. M., Cox, S. J., and the GENIE team: Multiobjective tuning of Grid-enabled Earth System Models using a Non-dominated Sorting Genetic Algorithm (NSGA-II), *Proceedings of the 2nd International Conference on eScience and Grid Computing*, Amsterdam, Netherlands, December, 2006.

Rahmstorf, S., Crucifix, M., Ganopolski, A., Goosse, H., Kamenkovich, I., Knutti, R.,

The “genie_eb_go_gs” configuration of GENIE

R. Marsh et al.

[Title Page](#)

[Abstract](#)

[Introduction](#)

[Conclusions](#)

[References](#)

[Tables](#)

[Figures](#)

◀

▶

◀

▶

[Back](#)

[Close](#)

[Full Screen / Esc](#)

[Printer-friendly Version](#)

[Interactive Discussion](#)



The “genie_eb_go_gs” configuration of GENIE

R. Marsh et al.

Table 1. Mesh-specific files required for `genie_eb_go_gs` on `<world>` mesh.

File	Purpose	Source
<code><world>.k1</code>	Land-sea mask, plus catchment	User-defined
<code><world>.psiles</code>	Land-sea mask and island index for barotropic streamfunction	Derived from <code><world>.k1</code>
<code><world>.paths</code>	Island boundary data for barotropic streamfunction	Derived from <code><world>.k1</code>
<code><world>.uncep</code>	Zonal moisture advection field	NCEP/NCAR reanalysis
<code><world>.vncep</code>	Meridional moisture advection field	NCEP/NCAR reanalysis
<code><world>.taux_u_interp</code>	Ocean wind-stress component	NOC climatology
<code><world>.taux_v_interp</code>	Ocean wind-stress component	NOC climatology
<code><world>.tauy_u_interp</code>	Ocean wind-stress component	NOC climatology
<code><world>.tauy_v_interp</code>	Ocean wind-stress component	NOC climatology
<code><world>.tempann</code>	Observational ocean temperature data for error estimation	NCEP/NCAR reanalysis
<code><world>.saliann</code>	Observational ocean salinity data for error estimation	NCEP/NCAR reanalysis
<code><world>.ta</code>	Observational air temperature data for error estimation	NCEP/NCAR reanalysis
<code><world>.qa</code>	Observational humidity data for error estimation	NCEP/NCAR reanalysis

[Title Page](#)

[Abstract](#)

[Introduction](#)

[Conclusions](#)

[References](#)

[Tables](#)

[Figures](#)

◀

▶

◀

▶

[Back](#)

[Close](#)

[Full Screen / Esc](#)

[Printer-friendly Version](#)

[Interactive Discussion](#)



The “genie_eb_go_gs” configuration of GENIE

R. Marsh et al.

Table 2. Common constants (see `genie-main/genie_global.f90`).

Constant	Value	Units
Year length	365.25	days
Radius of Earth	6370×10^3	m

[Title Page](#)

[Abstract](#)

[Introduction](#)

[Conclusions](#)

[References](#)

[Tables](#)

[Figures](#)

◀

▶

◀

▶

[Back](#)

[Close](#)

[Full Screen / Esc](#)

[Printer-friendly Version](#)

[Interactive Discussion](#)



The “genie_eb_gs” configuration of GENIE

R. Marsh et al.

Table 3. Constants (Ocean).

Constant	Value	Units
Density of pure water	1000	kg m^{-3}
Reference salinity	34.9	psu
Heat capacity of seawater	3981.1	$\text{J kg}^{-1} \text{K}^{-1}$

[Title Page](#)

[Abstract](#)

[Introduction](#)

[Conclusions](#)

[References](#)

[Tables](#)

[Figures](#)



[Back](#)

[Close](#)

[Full Screen / Esc](#)

[Printer-friendly Version](#)

[Interactive Discussion](#)



Table 4. Constants (Atmosphere, with simplest land scheme).

Constant	Value	Units
Stefan-Boltzmann constant	1000	$\text{W m}^{-2} \text{K}^{-4}$
Solar constant	1368	W m^{-2}
Pre-industrial CO ₂	282.9	ppmv
Fractional absorption coefficient of shortwave radiation in the atmosphere (over ocean only)	0.3	Non-dimensional
Radiative forcing sensitivity	5.77	W m^{-2}
Air density	1.25	kg m^{-3}
Water density	1000	kg m^{-3}
Depth scale – heat	8400	m
Depth scale – moisture	1800	m
Heat capacity of air	1004	$\text{J kg}^{-1} \text{K}^{-1}$
Latent heat of vaporization	2.501×10^6	J kg^{-1}
Latent heat of fusion of ice	3.34×10^5	J kg^{-1}
Drag coefficient	0.0013	Non-dimensional

The “genie_eb_gos” configuration of GENIE

R. Marsh et al.

[Title Page](#)

[Abstract](#)

[Introduction](#)

[Conclusions](#)

[References](#)

[Tables](#)

[Figures](#)

◀

▶

◀

▶

[Back](#)

[Close](#)

[Full Screen / Esc](#)

[Printer-friendly Version](#)

[Interactive Discussion](#)



The “genie_eb_go_gs” configuration of GENIE

R. Marsh et al.

Table 5. Constants (Sea Ice).

Constant	Value	Units
Latent heat of fusion of ice	3.34×10^5	J kg ⁻¹
Specific heat of sea water under ice	4044	J kg ⁻¹ K ⁻¹
Representative ice density	913	kg m ⁻³

[Title Page](#)

[Abstract](#)

[Introduction](#)

[Conclusions](#)

[References](#)

[Tables](#)

[Figures](#)



[Back](#)

[Close](#)

[Full Screen / Esc](#)

[Printer-friendly Version](#)

[Interactive Discussion](#)



Table 6. Default values of key parameters (specified in `genie_main/ runtime_defaults.sh`).

Parameter	Default Value	Units
Horizontal diffusivity	2000	$\text{m}^2 \text{s}^{-1}$
Vertical diffusivity	10^{-5}	$\text{m}^2 \text{s}^{-1}$
Inverse frictional timescale	2.5	days ⁻¹
Wind stress scaling	2.0	non-dimensional
Amplitude of atmospheric heat diffusivity profile (at Equator)	5×10^6	$\text{m}^2 \text{s}^{-1}$
“Width” scale for atmospheric diffusivity profile	1.0	Radians
Meridional slope for atmospheric diffusivity profile	0.1	non-dimensional
Moisture diffusivity	10^6	$\text{m}^2 \text{s}^{-1}$
Advection coefficient for heat	0.0	non-dimensional
Advection coefficient for moisture	0.4	non-dimensional
Additional net freshwater flux from Atlantic to Pacific sector	0.32	Sv
Diffusivity of sea ice thickness and concentration	2000	$\text{m}^2 \text{s}^{-1}$

The “genie_eb_gos” configuration of GENIE

R. Marsh et al.

[Title Page](#)

[Abstract](#)

[Introduction](#)

[Conclusions](#)

[References](#)

[Tables](#)

[Figures](#)

◀

▶

◀

▶

[Back](#)

[Close](#)

[Full Screen / Esc](#)

[Printer-friendly Version](#)

[Interactive Discussion](#)



The “genie_eb_go_gs” configuration of GENIE

R. Marsh et al.

Table 7. Configuration files (in `genie-main/configs`) used in experiments reported here. For the four standard climate experiments, only the 64×32 mesh files are listed, for brevity. Files specific to the other three meshes are named according to the protocol for the spin-up experiments.

Experiment	Length (years)	Configuration Filename
36×36 s spin-up	4000	<code>genie_eb_go_gs_4k.config</code>
72×72 s spin-up	4000	<code>genie_eb_go_gs_7272_4k.config</code>
36×60 spin-up	4000	<code>genie_eb_go_gs_3660_4k.config</code>
64×32 spin-up	4000	<code>genie_eb_go_gs_6432_4k.config</code>
64×32 equilibrium CO ₂ doubling	4000	<code>genie_eb_go_gs_6432_4k_2xCO2.config</code>
64×32 transient CO ₂ doubling	70	<code>genie_eb_go_gs_6432_4k_rest_CO2.config</code>
64×32 freshwater hosing	200	<code>genie_eb_go_gs_6432_4k_rest_FWF.config</code>
64×32 hysteresis	5000+5000	<code>genie_eb_go_gs_6432_4k_rest_hyst_forward.config</code> + <code>genie_eb_go_gs_6432_4k_rest_hyst_reverse.config</code>

[Title Page](#)

[Abstract](#)

[Introduction](#)

[Conclusions](#)

[References](#)

[Tables](#)

[Figures](#)

◀

▶

◀

▶

[Back](#)

[Close](#)

[Full Screen / Esc](#)

[Printer-friendly Version](#)

[Interactive Discussion](#)



The “genie_eb_go_gs” configuration of GENIE

R. Marsh et al.

[Title Page](#)

[Abstract](#)

[Introduction](#)

[Conclusions](#)

[References](#)

[Tables](#)

[Figures](#)

◀

▶

◀

▶

[Back](#)

[Close](#)

[Full Screen / Esc](#)

[Printer-friendly Version](#)

[Interactive Discussion](#)



The “genie_eb_gos” configuration of GENIE

R. Marsh et al.

Table 9. Equilibrium climate sensitivity and transient climate response, for each mesh.

Mesh	Equilibrium Climate Sensitivity (°C)	Transient Climate Response (°C)
36×36 s	2.884	1.727
64×32	2.852	1.795
36×60	2.868	1.667
72×72 s	3.130	1.996

[Title Page](#)

[Abstract](#)

[Introduction](#)

[Conclusions](#)

[References](#)

[Tables](#)

[Figures](#)

◀

▶

◀

▶

[Back](#)

[Close](#)

[Full Screen / Esc](#)

[Printer-friendly Version](#)

[Interactive Discussion](#)



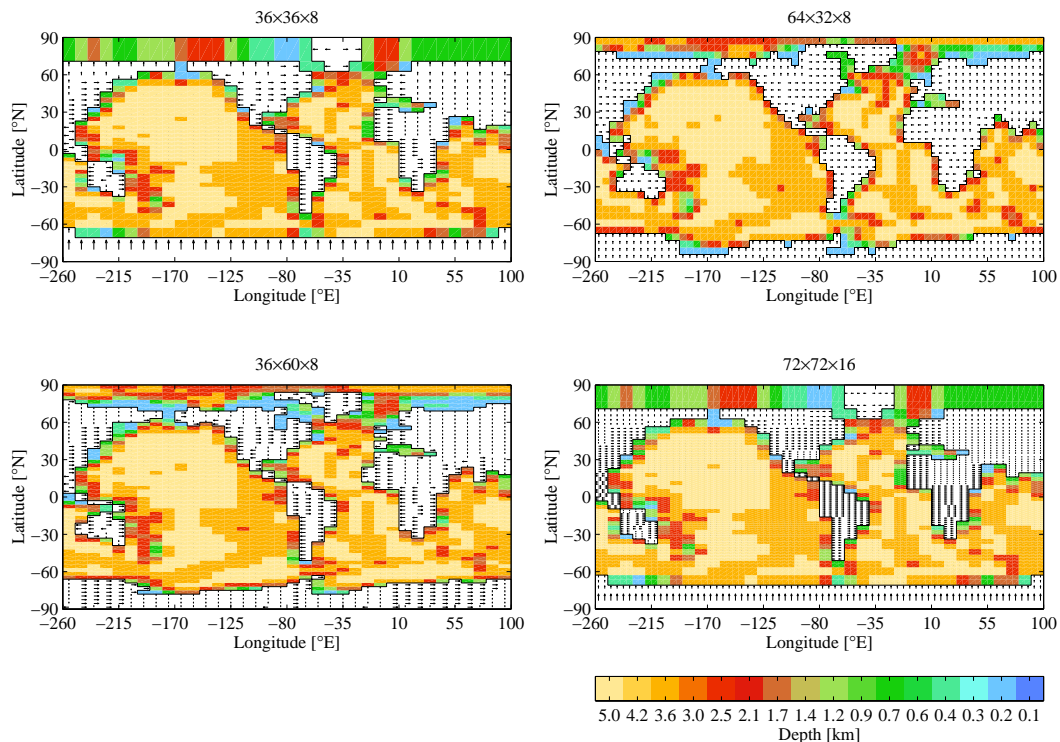


Fig. 1. Model ocean depth (km) at different resolution. The arrows on land indicate direction of runoff.

The “genie_eb_gs” configuration of GENIE

R. Marsh et al.

[Title Page](#)

[Abstract](#)

[Introduction](#)

[Conclusions](#)

[References](#)

[Tables](#)

[Figures](#)

◀

▶

◀

▶

[Back](#)

[Close](#)

[Full Screen / Esc](#)

[Printer-friendly Version](#)

[Interactive Discussion](#)



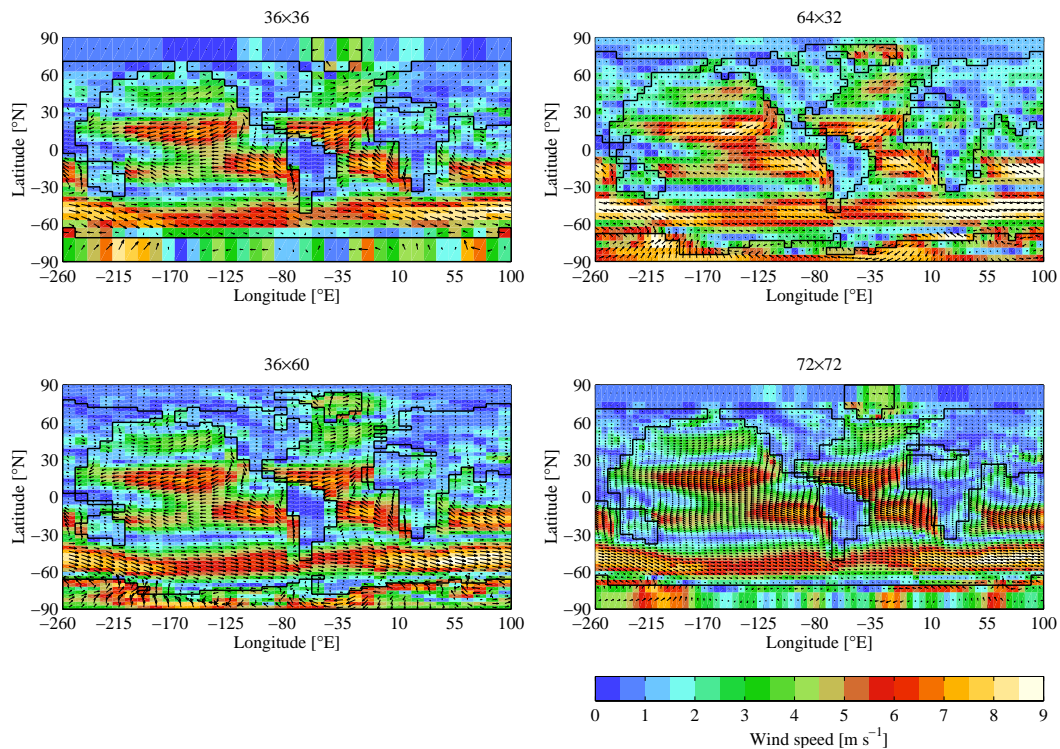


Fig. 2. Annual-mean wind direction and speed (m s^{-1}).

The “genie_eb_gos” configuration of GENIE

R. Marsh et al.

[Title Page](#)

[Abstract](#)

[Introduction](#)

[Conclusions](#)

[References](#)

[Tables](#)

[Figures](#)

◀

▶

◀

▶

[Back](#)

[Close](#)

[Full Screen / Esc](#)

[Printer-friendly Version](#)

[Interactive Discussion](#)



The “genie_eb_gogs” configuration of GENIE

R. Marsh et al.

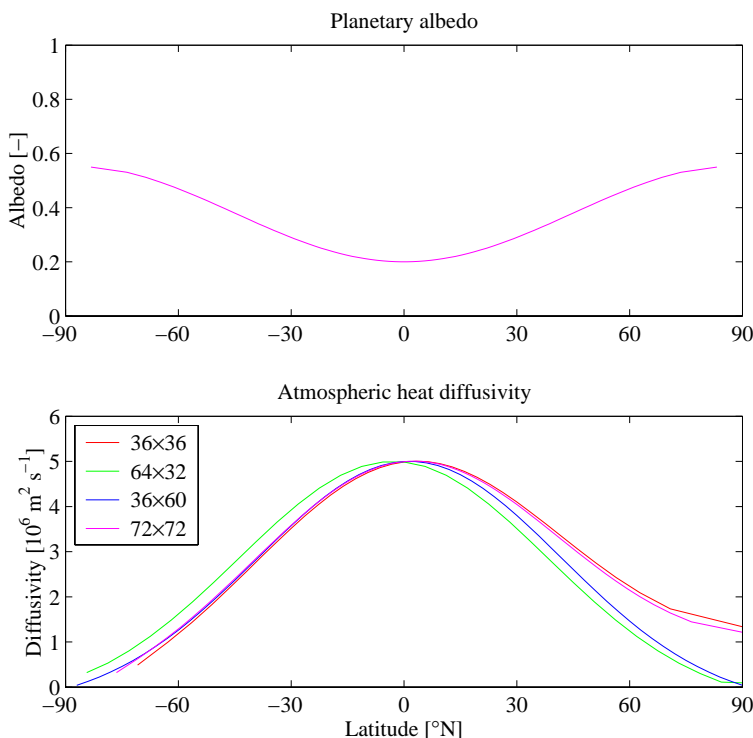


Fig. 3. Meridional profiles: **(a)** climatological albedo; **(b)** heat diffusivities ($\text{m}^2 \text{s}^{-1}$), for default parameter values.

[Title Page](#)

[Abstract](#)

[Introduction](#)

[Conclusions](#)

[References](#)

[Tables](#)

[Figures](#)

◀

▶

◀

▶

[Back](#)

[Close](#)

[Full Screen / Esc](#)

[Printer-friendly Version](#)

[Interactive Discussion](#)



The “genie_eb_gs” configuration of GENIE

R. Marsh et al.

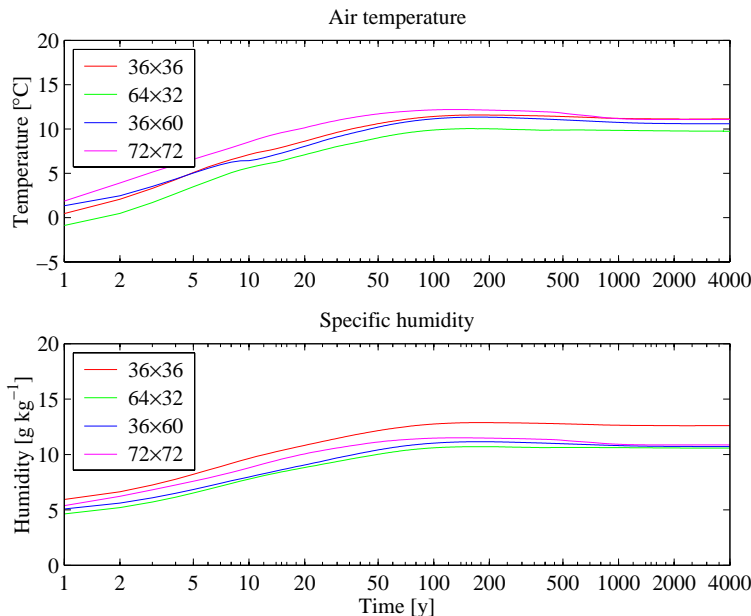


Fig. 4. Global-mean measures of model climate: **(a)** air temperature ($^{\circ}\text{C}$); **(b)** specific humidity (g kg^{-1}).

- [Title Page](#)
- [Abstract](#) [Introduction](#)
- [Conclusions](#) [References](#)
- [Tables](#) [Figures](#)
- [◀](#) [▶](#)
- [◀](#) [▶](#)
- [Back](#) [Close](#)
- [Full Screen / Esc](#)
- [Printer-friendly Version](#)
- [Interactive Discussion](#)

The “genie_eb_gos” configuration of GENIE

R. Marsh et al.

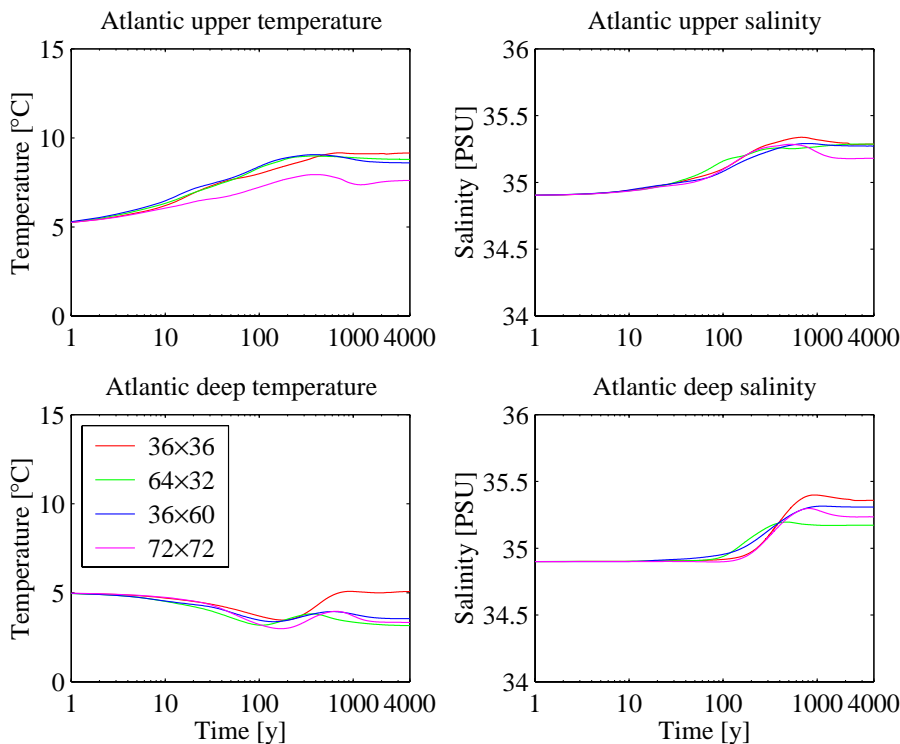


Fig. 5. Selected integral measures of averages in the Atlantic sector: **(a)** upper temperature (°C); **(b)** upper salinity (psu); **(c)** deep temperature (°C); **(d)** deep salinity (psu).

- [Title Page](#)
- [Abstract](#) [Introduction](#)
- [Conclusions](#) [References](#)
- [Tables](#) [Figures](#)
- [◀](#) [▶](#)
- [◀](#) [▶](#)
- [Back](#) [Close](#)
- [Full Screen / Esc](#)
- [Printer-friendly Version](#)
- [Interactive Discussion](#)

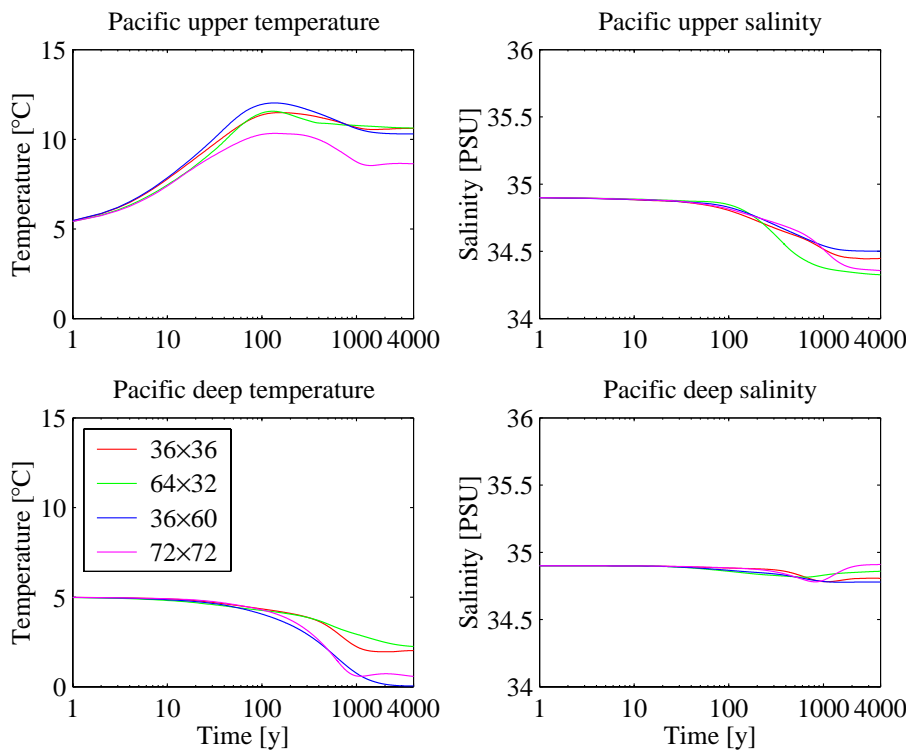


Fig. 6. As Fig. 5, for the Pacific sector.

The “genie_eb_gos” configuration of GENIE

R. Marsh et al.

[Title Page](#)

[Abstract](#)

[Introduction](#)

[Conclusions](#)

[References](#)

[Tables](#)

[Figures](#)

◀

▶

◀

▶

[Back](#)

[Close](#)

[Full Screen / Esc](#)

[Printer-friendly Version](#)

[Interactive Discussion](#)



The “genie_eb_go_gs” configuration of GENIE

R. Marsh et al.

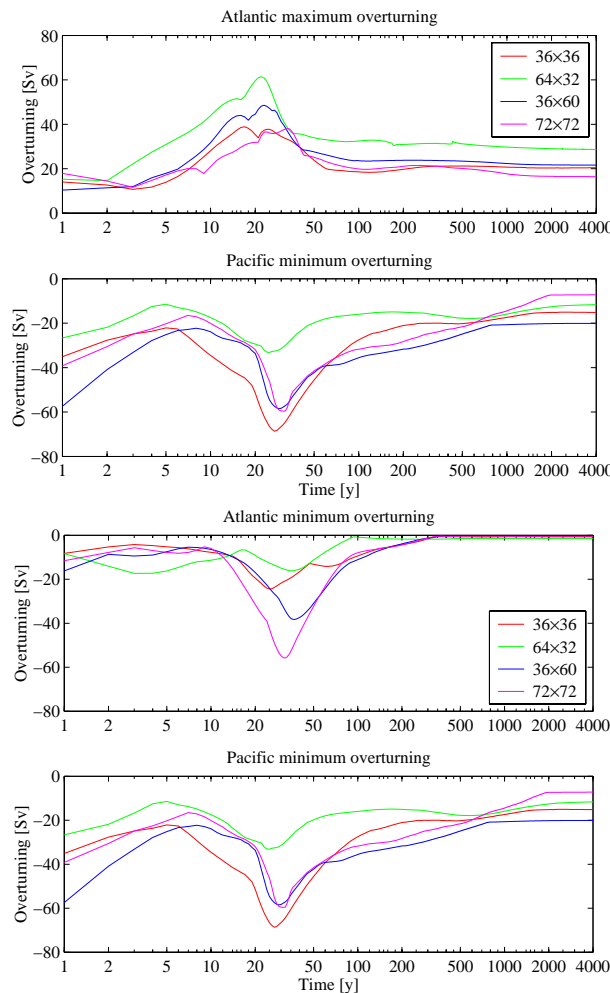


Fig. 7. Maxima and minima of overturning rates (Sv): **(a)** Atlantic; **(b)** Pacific.

[Title Page](#)

[Abstract](#)

[Introduction](#)

[Conclusions](#)

[References](#)

[Tables](#)

[Figures](#)

[◀](#)

[▶](#)

[◀](#)

[▶](#)

[Back](#)

[Close](#)

[Full Screen / Esc](#)

[Printer-friendly Version](#)

[Interactive Discussion](#)

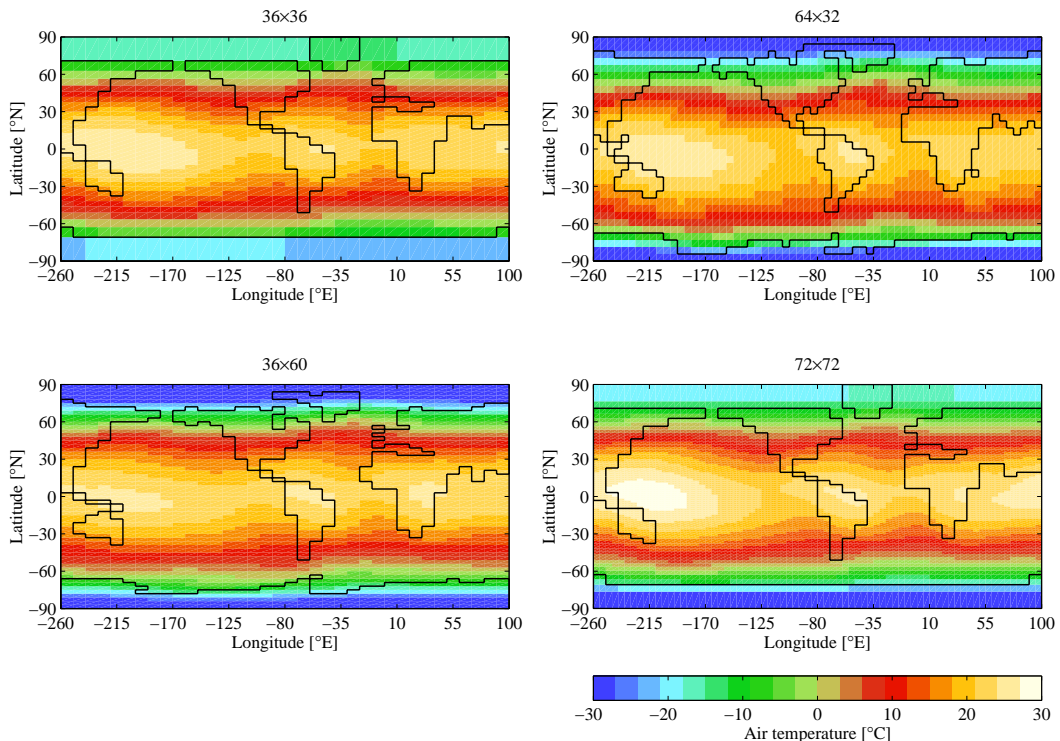


Fig. 8. Maps of annual-mean air temperature (°C).

The “genie_eb_go_gs” configuration of GENIE

R. Marsh et al.

[Title Page](#)

[Abstract](#)

[Introduction](#)

[Conclusions](#)

[References](#)

[Tables](#)

[Figures](#)

◀

▶

◀

▶

[Back](#)

[Close](#)

[Full Screen / Esc](#)

[Printer-friendly Version](#)

[Interactive Discussion](#)



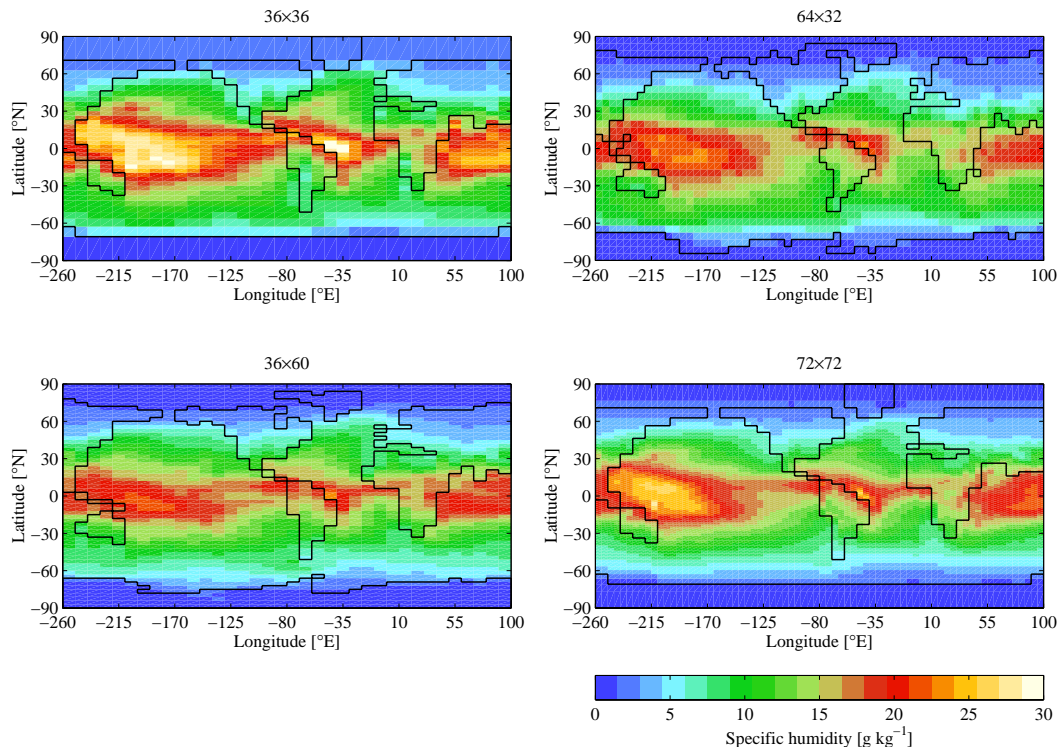


Fig. 9. Maps of annual-mean specific humidity (g kg^{-1}).

The “genie_eb_gos” configuration of GENIE

R. Marsh et al.

[Title Page](#)

[Abstract](#)

[Introduction](#)

[Conclusions](#)

[References](#)

[Tables](#)

[Figures](#)

◀

▶

◀

▶

[Back](#)

[Close](#)

[Full Screen / Esc](#)

[Printer-friendly Version](#)

[Interactive Discussion](#)



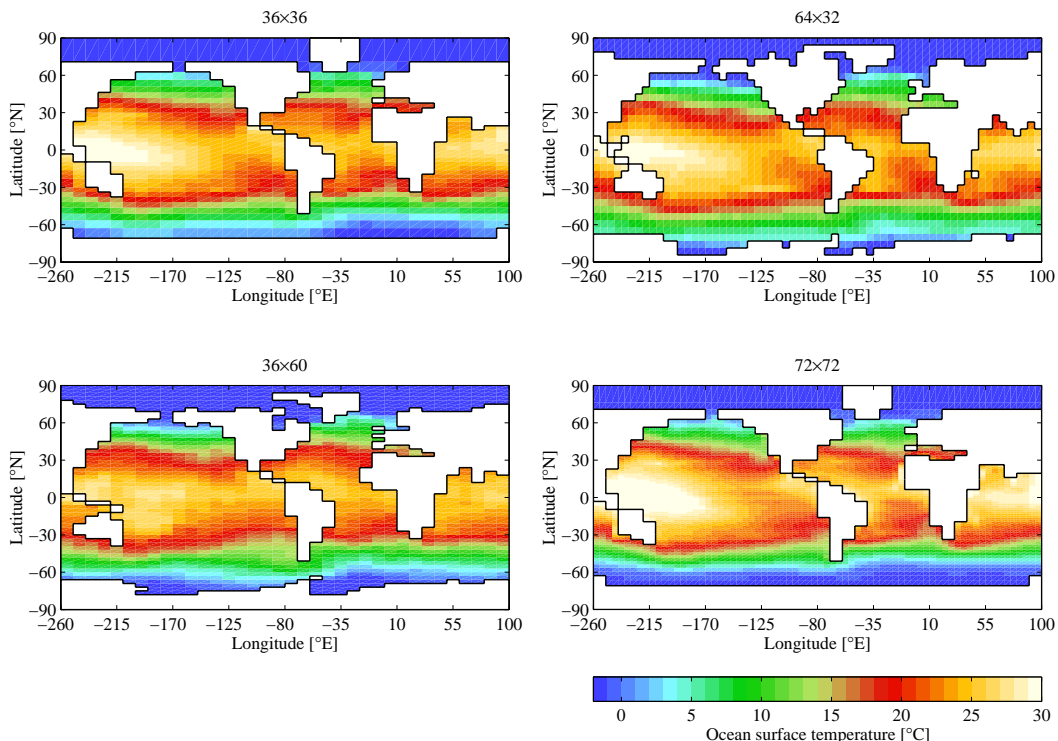


Fig. 10. Maps of annual-mean ocean surface temperature (°C).

The “genie_eb_gs” configuration of GENIE

R. Marsh et al.

[Title Page](#)

[Abstract](#)

[Introduction](#)

[Conclusions](#)

[References](#)

[Tables](#)

[Figures](#)

◀

▶

◀

▶

[Back](#)

[Close](#)

[Full Screen / Esc](#)

[Printer-friendly Version](#)

[Interactive Discussion](#)



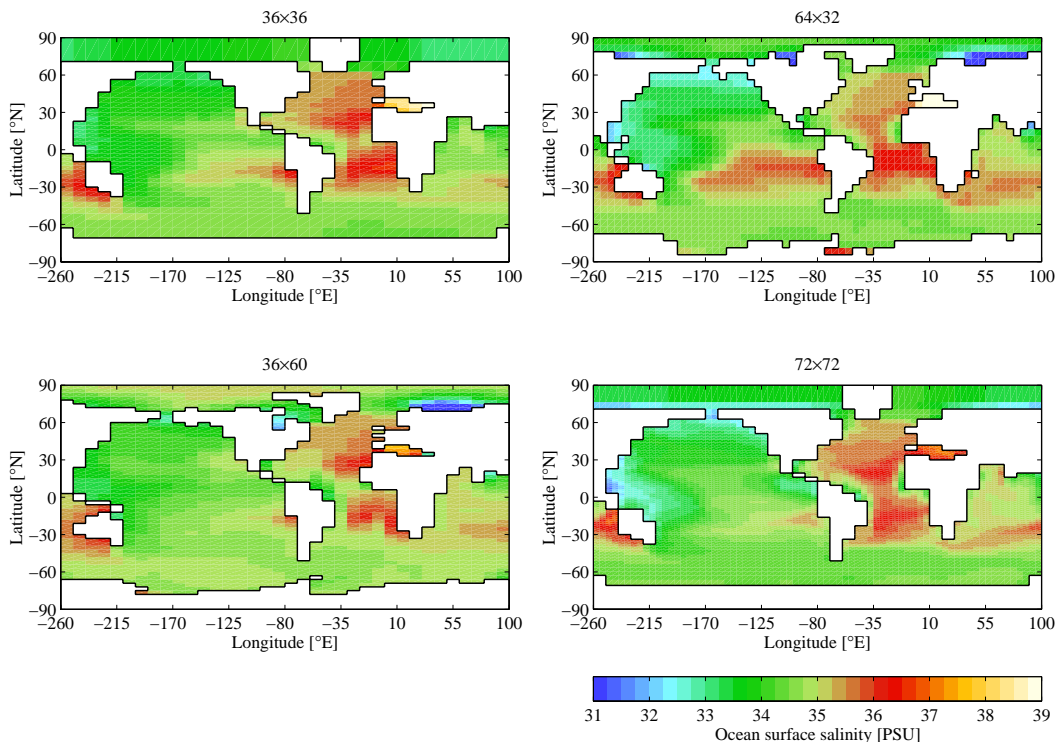


Fig. 11. Maps of annual-mean ocean surface salinity (psu).

The “genie_eb_gos” configuration of GENIE

R. Marsh et al.

[Title Page](#)

[Abstract](#)

[Introduction](#)

[Conclusions](#)

[References](#)

[Tables](#)

[Figures](#)

◀

▶

◀

▶

[Back](#)

[Close](#)

[Full Screen / Esc](#)

[Printer-friendly Version](#)

[Interactive Discussion](#)



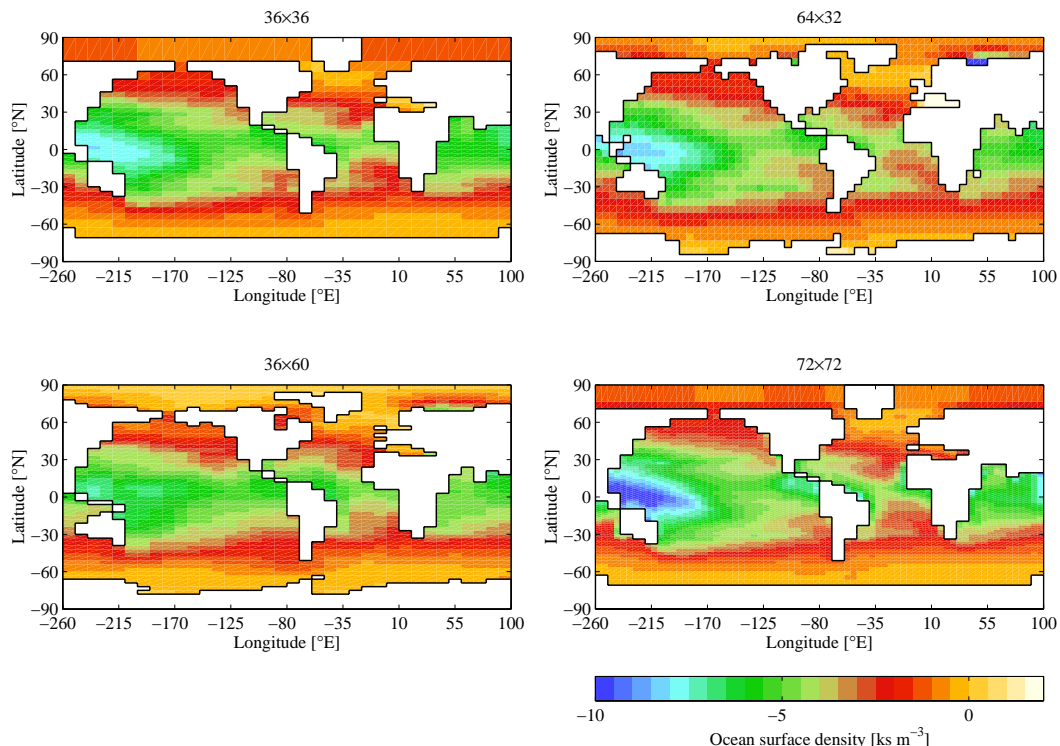


Fig. 12. Maps of annual-mean ocean surface density anomaly (kg m^{-3}).

The “genie_eb_go_gs” configuration of GENIE

R. Marsh et al.

[Title Page](#)

[Abstract](#)

[Introduction](#)

[Conclusions](#)

[References](#)

[Tables](#)

[Figures](#)

◀

▶

◀

▶

[Back](#)

[Close](#)

[Full Screen / Esc](#)

[Printer-friendly Version](#)

[Interactive Discussion](#)



The “genie_eb_gos” configuration of GENIE

R. Marsh et al.

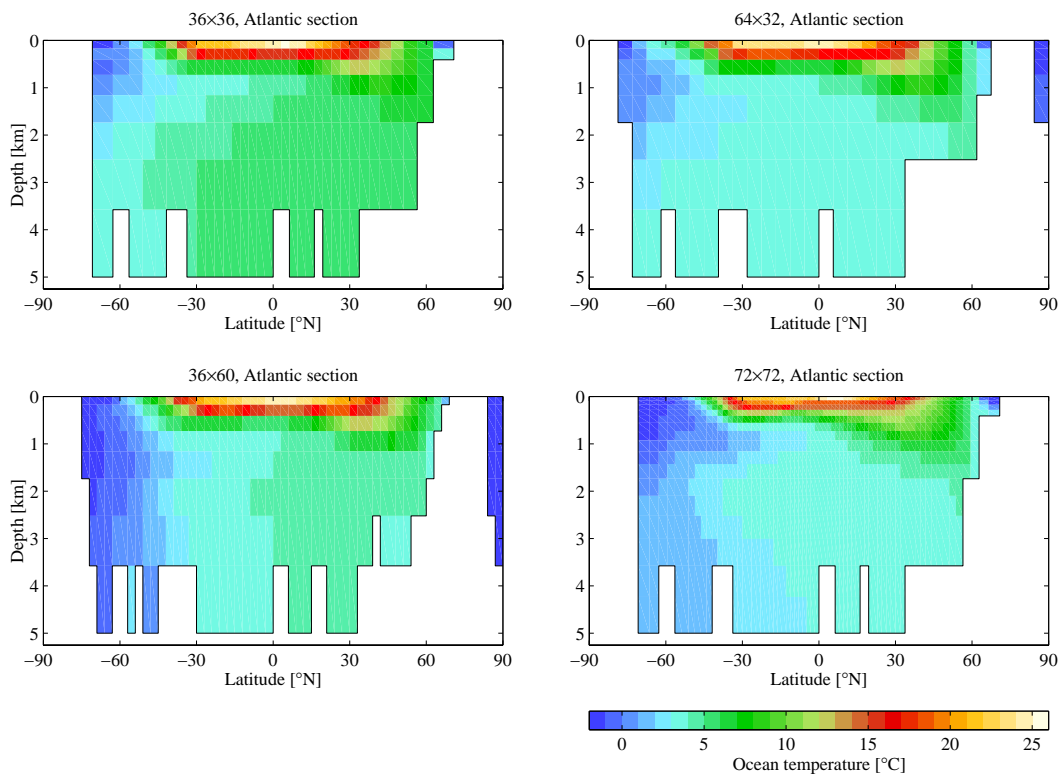


Fig. 13. Meridional sections of annual-mean temperature through the central Atlantic.

Printer-friendly Version

Interactive Discussion

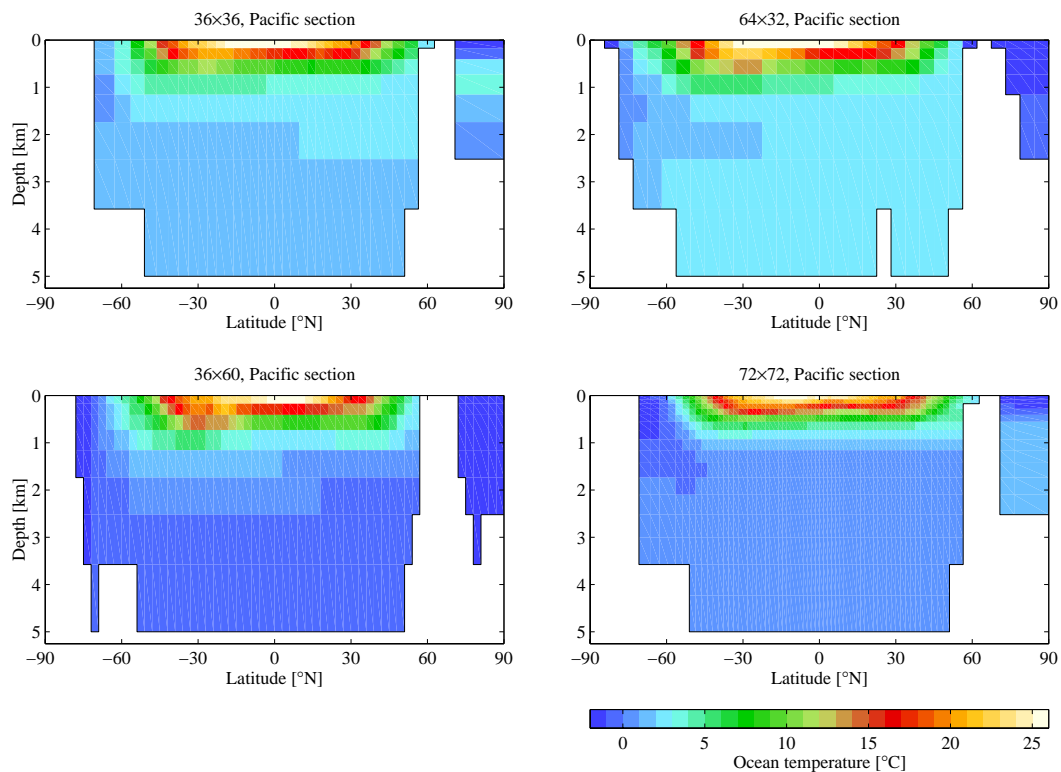


Fig. 14. Meridional sections of annual-mean temperature through the central Pacific.

The “genie_eb_gos” configuration of GENIE

R. Marsh et al.

[Title Page](#)

[Abstract](#)

[Introduction](#)

[Conclusions](#)

[References](#)

[Tables](#)

[Figures](#)

◀

▶

◀

▶

[Back](#)

[Close](#)

[Full Screen / Esc](#)

[Printer-friendly Version](#)

[Interactive Discussion](#)



The “genie_eb_gos” configuration of GENIE

R. Marsh et al.

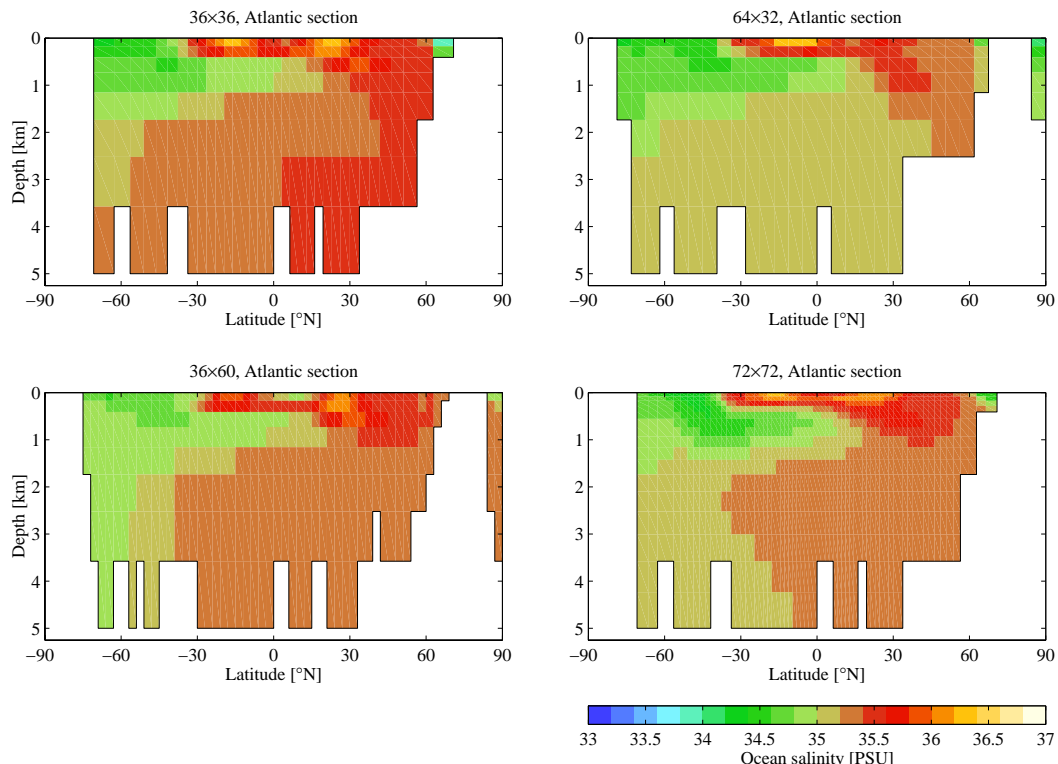


Fig. 15. Meridional sections of annual-mean salinity through the central Atlantic.

[Title Page](#)

[Abstract](#)

[Introduction](#)

[Conclusions](#)

[References](#)

[Tables](#)

[Figures](#)

◀

▶

◀

▶

[Back](#)

[Close](#)

[Full Screen / Esc](#)

[Printer-friendly Version](#)

[Interactive Discussion](#)



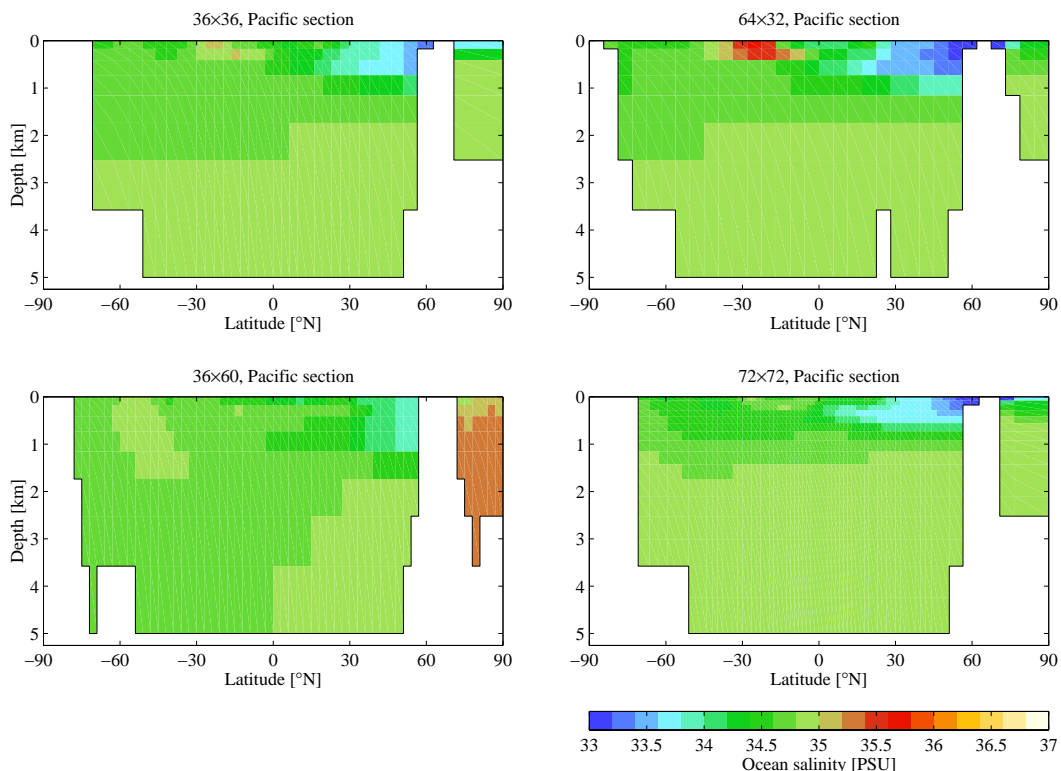


Fig. 16. Meridional sections of annual-mean salinity through the central Pacific.

The “genie_eb_gos” configuration of GENIE

R. Marsh et al.

[Title Page](#)

[Abstract](#)

[Introduction](#)

[Conclusions](#)

[References](#)

[Tables](#)

[Figures](#)

◀

▶

◀

▶

[Back](#)

[Close](#)

[Full Screen / Esc](#)

[Printer-friendly Version](#)

[Interactive Discussion](#)



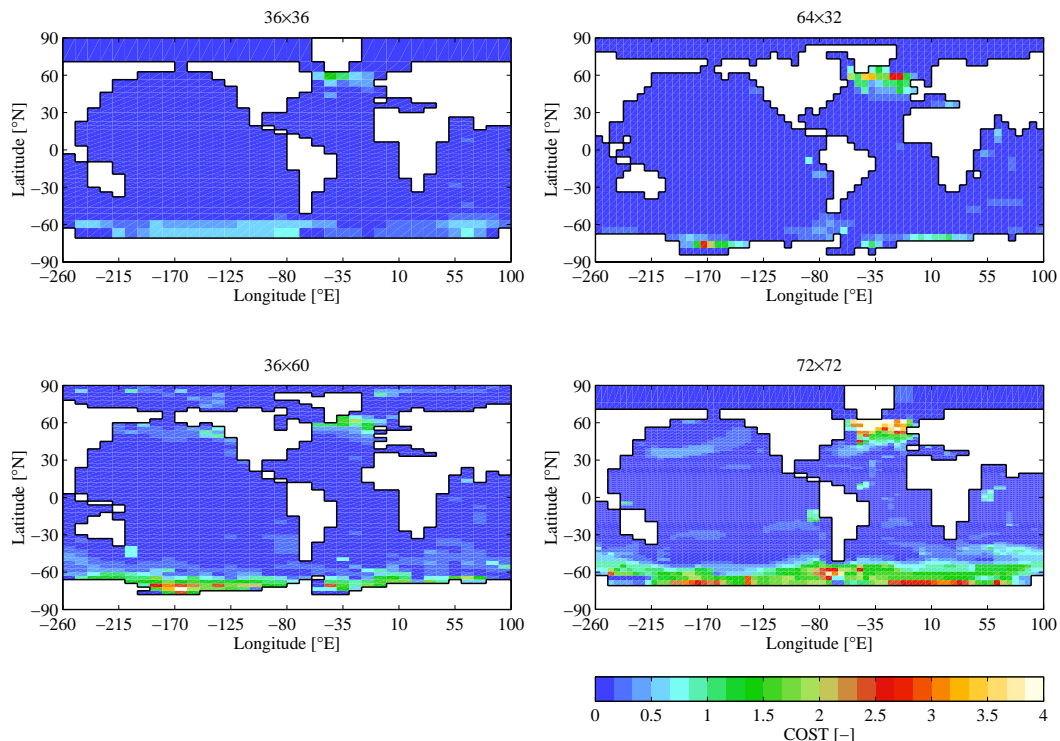


Fig. 17. Average convection depth level (note that these are depth level indices, not actual depths).

The “genie_eb_go_gs” configuration of GENIE

R. Marsh et al.

[Title Page](#)

[Abstract](#)

[Introduction](#)

[Conclusions](#)

[References](#)

[Tables](#)

[Figures](#)

◀

▶

◀

▶

[Back](#)

[Close](#)

[Full Screen / Esc](#)

[Printer-friendly Version](#)

[Interactive Discussion](#)



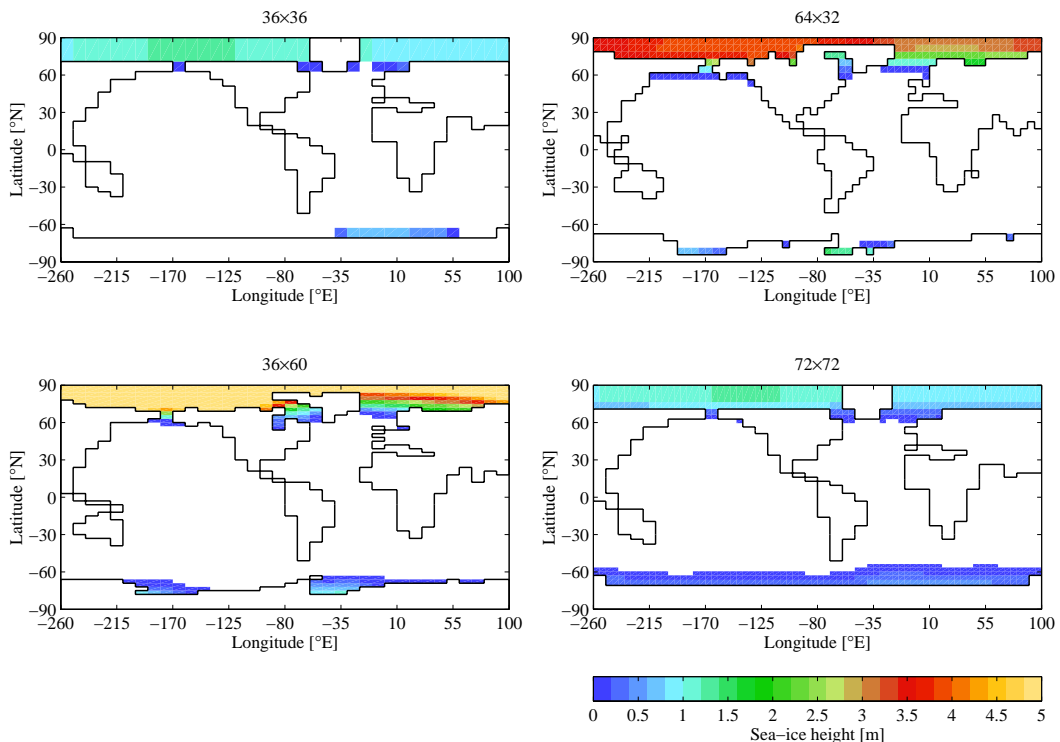


Fig. 18. Maps of annual-mean sea ice thickness (m).

The “genie_eb_gos” configuration of GENIE

R. Marsh et al.

[Title Page](#)

[Abstract](#)

[Introduction](#)

[Conclusions](#)

[References](#)

[Tables](#)

[Figures](#)

◀

▶

◀

▶

[Back](#)

[Close](#)

[Full Screen / Esc](#)

[Printer-friendly Version](#)

[Interactive Discussion](#)



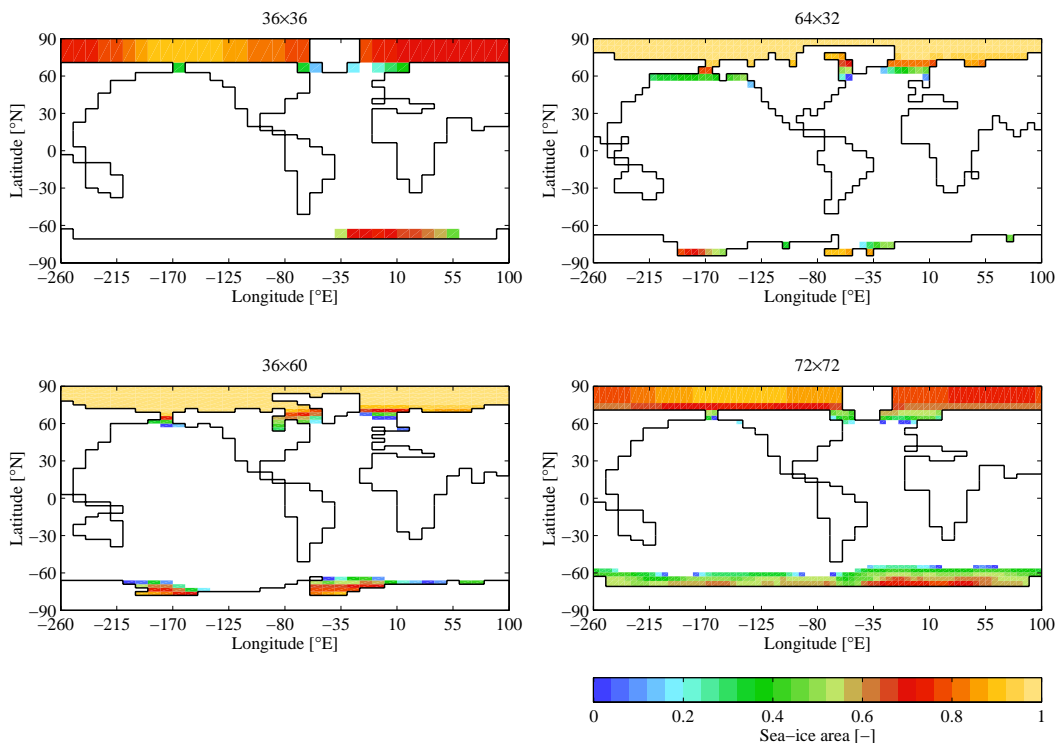


Fig. 19. Maps of annual-mean sea ice concentration.

The “genie_eb_gogs” configuration of GENIE

R. Marsh et al.

[Title Page](#)

[Abstract](#)

[Introduction](#)

[Conclusions](#)

[References](#)

[Tables](#)

[Figures](#)

◀

▶

◀

▶

[Back](#)

[Close](#)

[Full Screen / Esc](#)

[Printer-friendly Version](#)

[Interactive Discussion](#)



The “genie_eb_gs” configuration of GENIE

R. Marsh et al.

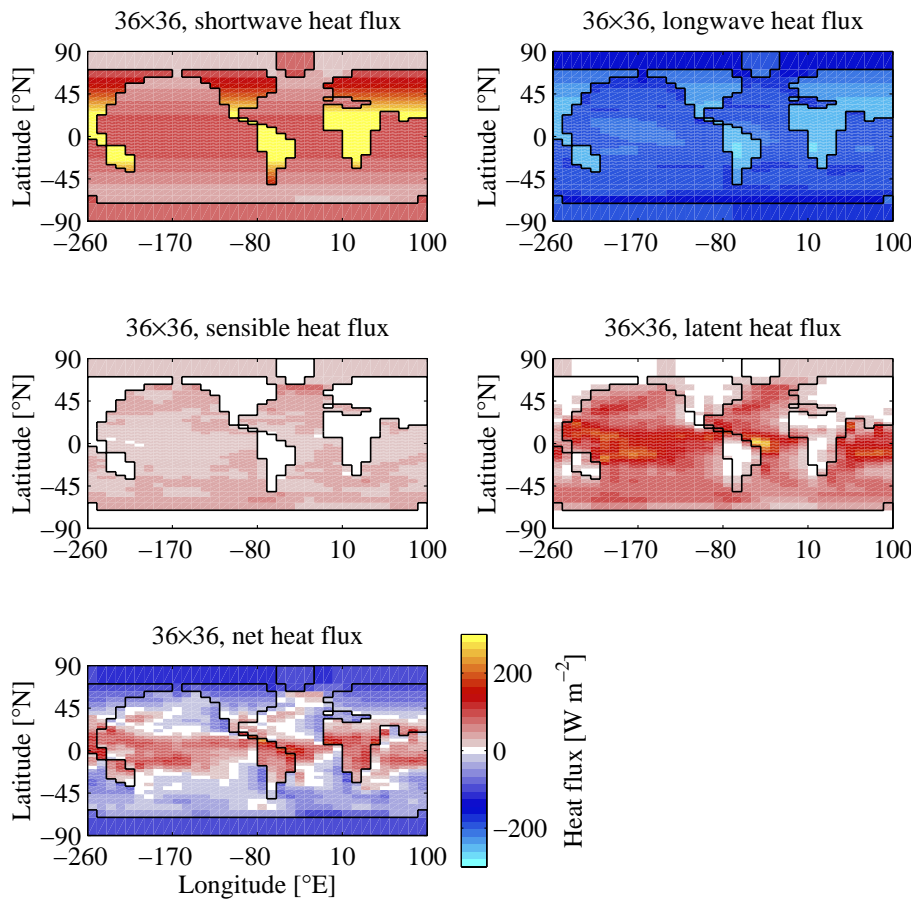


Fig. 20. Maps of annual-mean components of heat flux into the atmosphere, W m^{-2} (36×36 s mesh).

The “genie_eb_gs” configuration of GENIE

R. Marsh et al.

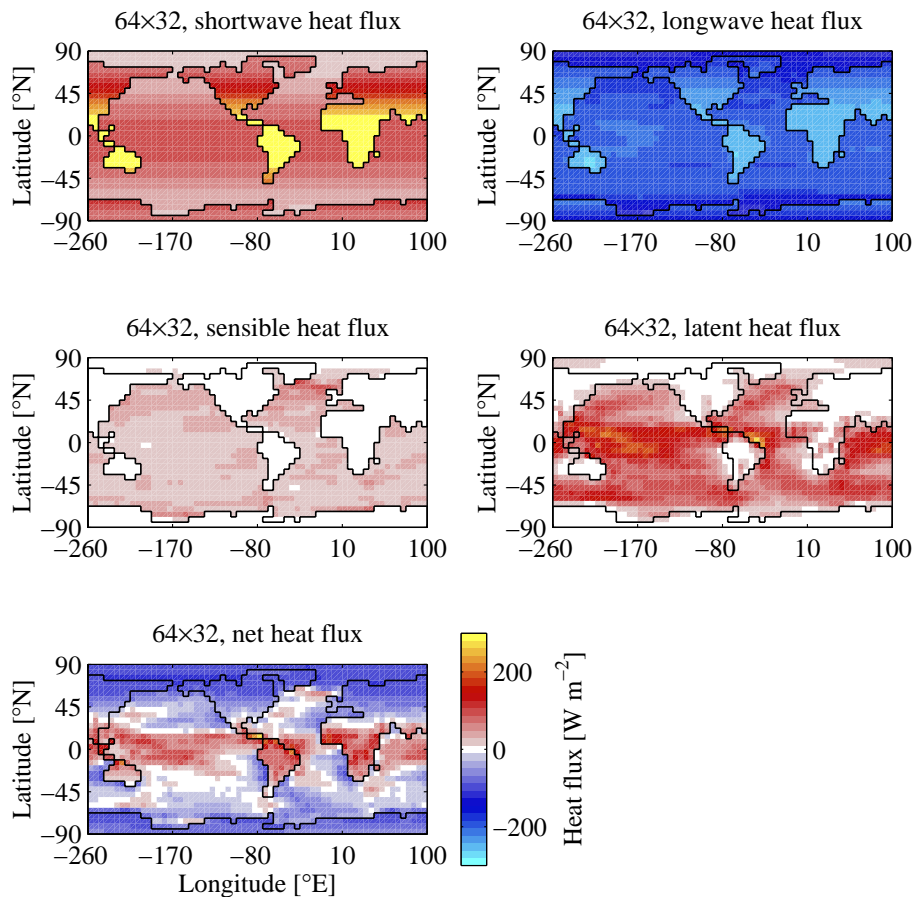


Fig. 21. Maps of annual-mean components of heat flux into the atmosphere, W m^{-2} (64×32 mesh).

Printer-friendly Version

Interactive Discussion

Tables Figures

◀ ▶

◀ ▶

Back Close

Full Screen / Esc

The “genie_eb_gs” configuration of GENIE

R. Marsh et al.

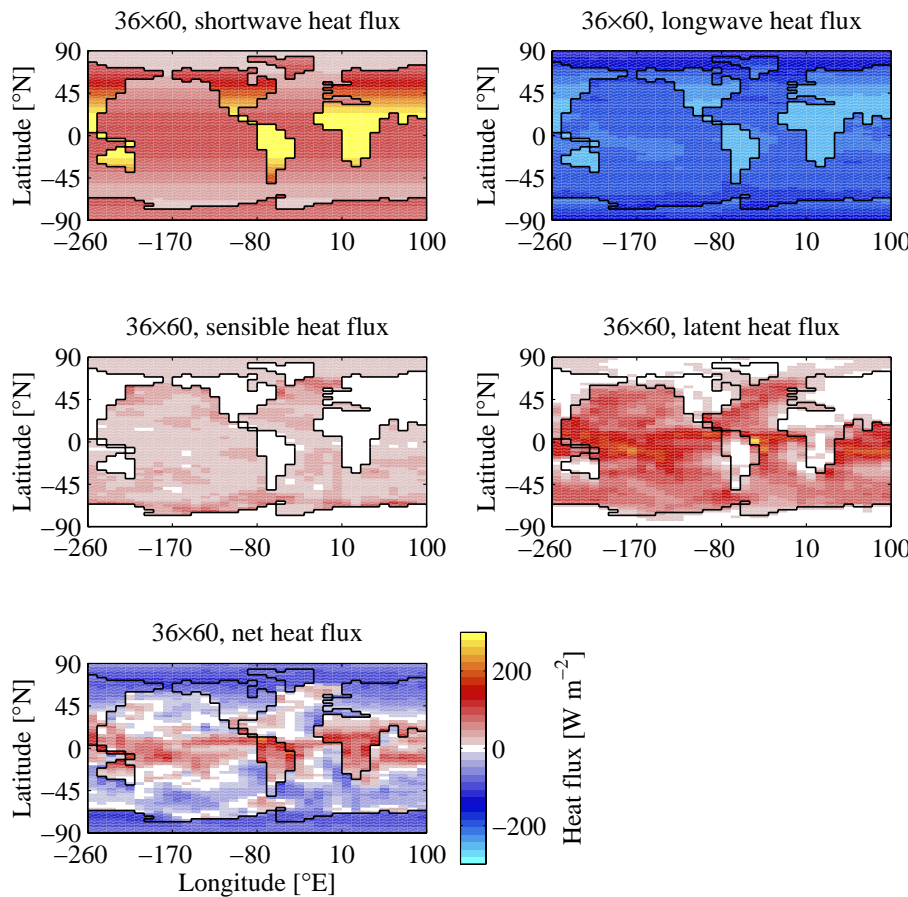


Fig. 22. Maps of annual-mean components of heat flux into the atmosphere, W m^{-2} (36×60 mesh).

[Title Page](#)[Abstract](#)[Introduction](#)[Conclusions](#)[References](#)[Tables](#)[Figures](#)[◀](#)[▶](#)[◀](#)[▶](#)[Back](#)[Close](#)[Full Screen / Esc](#)[Printer-friendly Version](#)[Interactive Discussion](#)

The “genie_eb_gs” configuration of GENIE

R. Marsh et al.

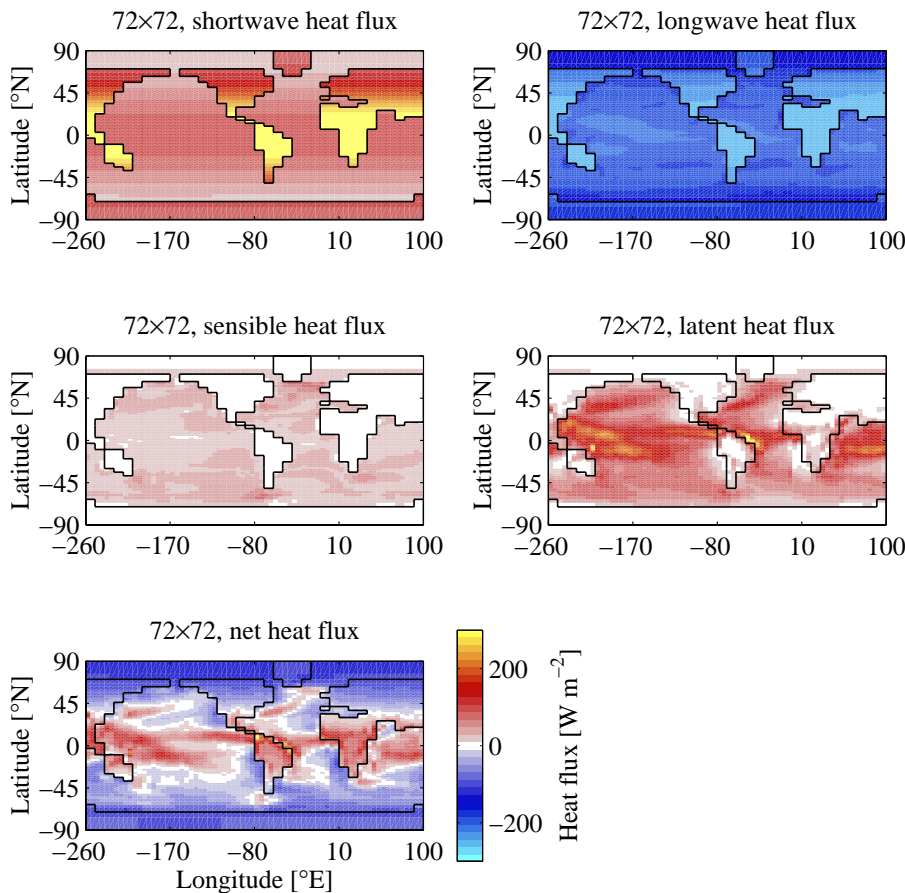


Fig. 23. Maps of annual-mean components of heat flux into the atmosphere, W m^{-2} (72×72 s mesh).

- [Title Page](#)
- [Abstract](#) [Introduction](#)
- [Conclusions](#) [References](#)
- [Tables](#) [Figures](#)
- [◀](#) [▶](#)
- [◀](#) [▶](#)
- [Back](#) [Close](#)
- [Full Screen / Esc](#)
- [Printer-friendly Version](#)
- [Interactive Discussion](#)

The “genie_eb_gs” configuration of GENIE

R. Marsh et al.

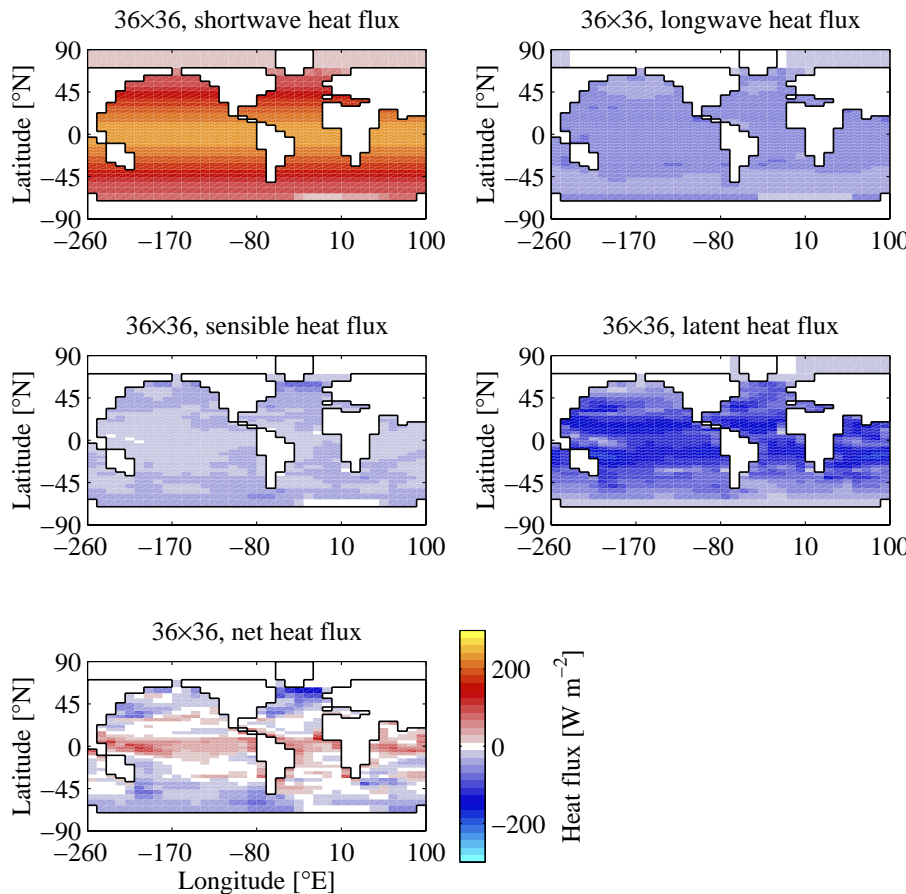


Fig. 24. Maps of annual-mean components of surface heat flux into the ocean, W m^{-2} (36×36 s mesh).

[Title Page](#)

[Abstract](#)

[Introduction](#)

[Conclusions](#)

[References](#)

[Tables](#)

[Figures](#)

◀

▶

◀

▶

[Back](#)

[Close](#)

[Full Screen / Esc](#)

[Printer-friendly Version](#)

[Interactive Discussion](#)



The “genie_eb_gs” configuration of GENIE

R. Marsh et al.

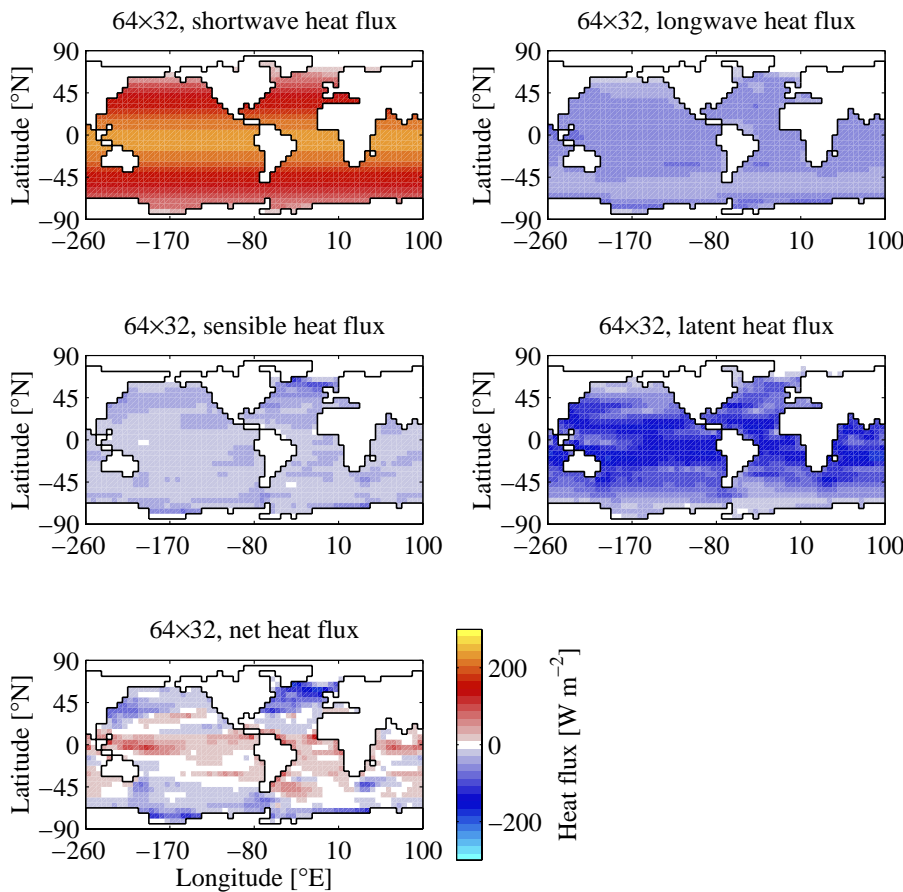


Fig. 25. Maps of annual-mean components of surface heat flux into the ocean, W m^{-2} (64×32 mesh).

[Title Page](#)[Abstract](#)[Introduction](#)[Conclusions](#)[References](#)[Tables](#)[Figures](#)[◀](#)[▶](#)[◀](#)[▶](#)[Back](#)[Close](#)[Full Screen / Esc](#)[Printer-friendly Version](#)[Interactive Discussion](#)

The “genie_eb_gs” configuration of GENIE

R. Marsh et al.

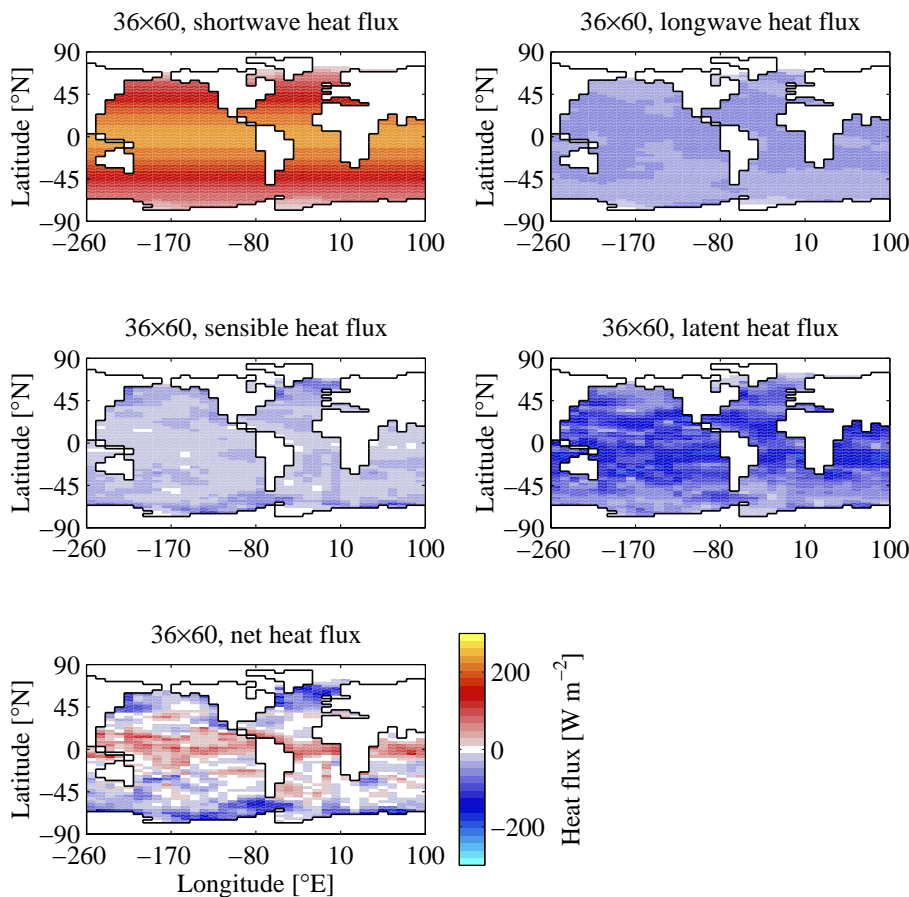


Fig. 26. Maps of annual-mean components of surface heat flux into the ocean, W m^{-2} (36×60 mesh).

[Title Page](#)[Abstract](#)[Introduction](#)[Conclusions](#)[References](#)[Tables](#)[Figures](#)[◀](#)[▶](#)[◀](#)[▶](#)[Back](#)[Close](#)[Full Screen / Esc](#)[Printer-friendly Version](#)[Interactive Discussion](#)

The “genie_eb_gs” configuration of GENIE

R. Marsh et al.

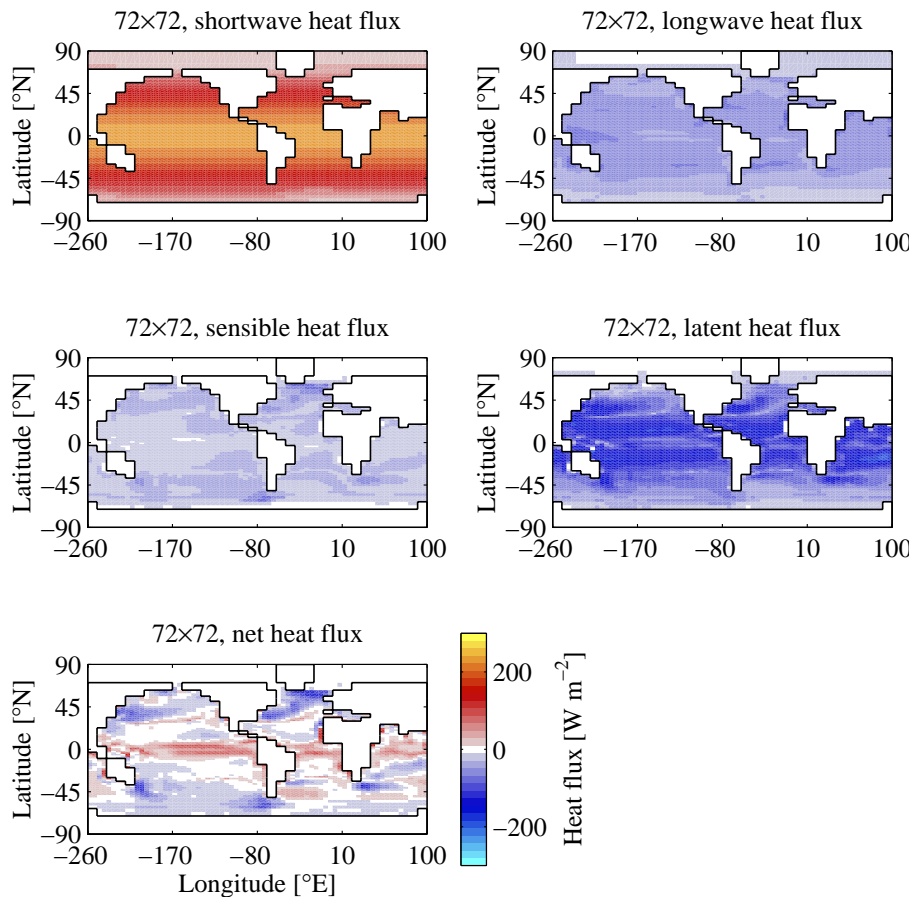


Fig. 27. Maps of annual-mean components of surface heat flux into the ocean, W m^{-2} (72×72 s mesh).

[Title Page](#)

[Abstract](#)

[Introduction](#)

[Conclusions](#)

[References](#)

[Tables](#)

[Figures](#)

◀

▶

◀

▶

[Back](#)

[Close](#)

[Full Screen / Esc](#)

[Printer-friendly Version](#)

[Interactive Discussion](#)



The “genie_eb_gogs” configuration of GENIE

R. Marsh et al.

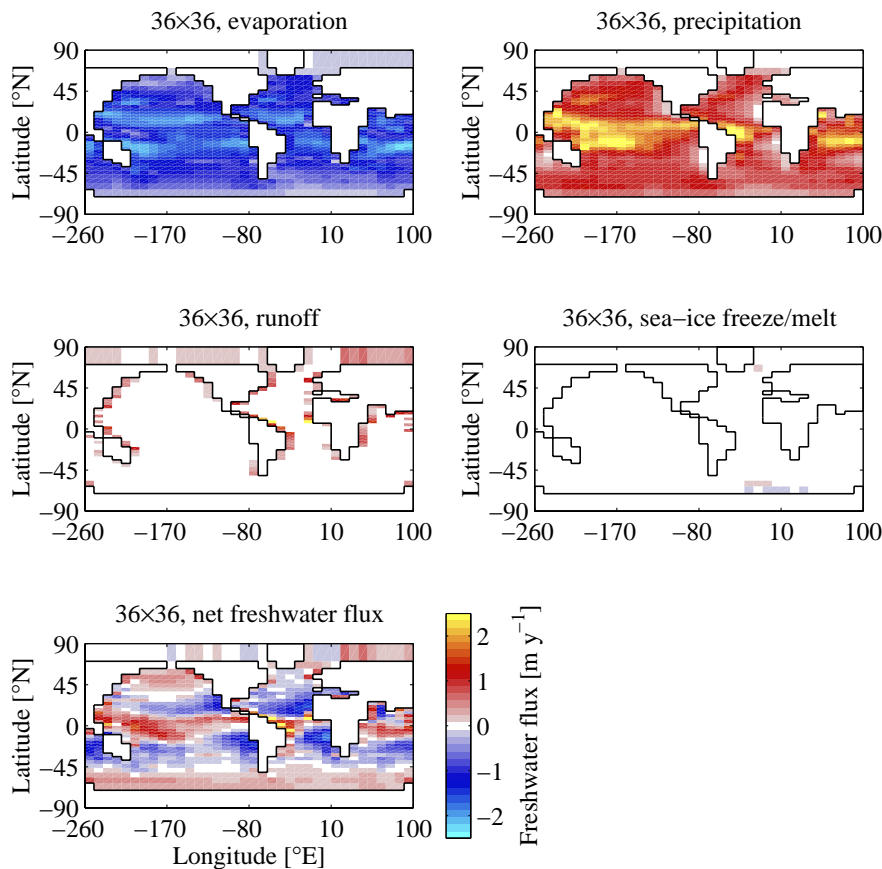


Fig. 28. Maps of annual-mean components of freshwater flux into the ocean, m y^{-1} (36×36 s mesh).

[Title Page](#)
[Abstract](#) [Introduction](#)
[Conclusions](#) [References](#)
[Tables](#) [Figures](#)

[◀◀](#) [▶▶](#)
[◀](#) [▶](#)
[Back](#) [Close](#)
[Full Screen / Esc](#)

[Printer-friendly Version](#)
[Interactive Discussion](#)



The “genie_eb_gogs” configuration of GENIE

R. Marsh et al.

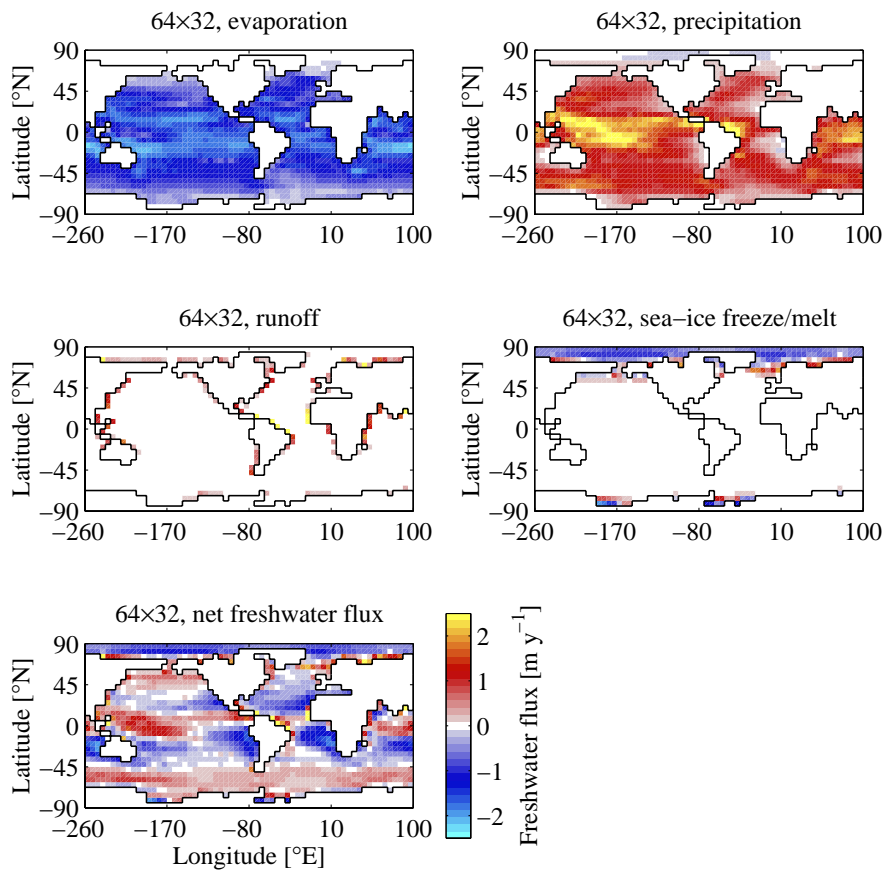


Fig. 29. Maps of annual-mean components of freshwater flux into the ocean, m y^{-1} (64x32 mesh).

[Title Page](#)
[Abstract](#) [Introduction](#)
[Conclusions](#) [References](#)
[Tables](#) [Figures](#)

[◀](#) [▶](#)
[◀](#) [▶](#)
[Back](#) [Close](#)
[Full Screen / Esc](#)

[Printer-friendly Version](#)
[Interactive Discussion](#)

The “genie_eb_gogs” configuration of GENIE

R. Marsh et al.

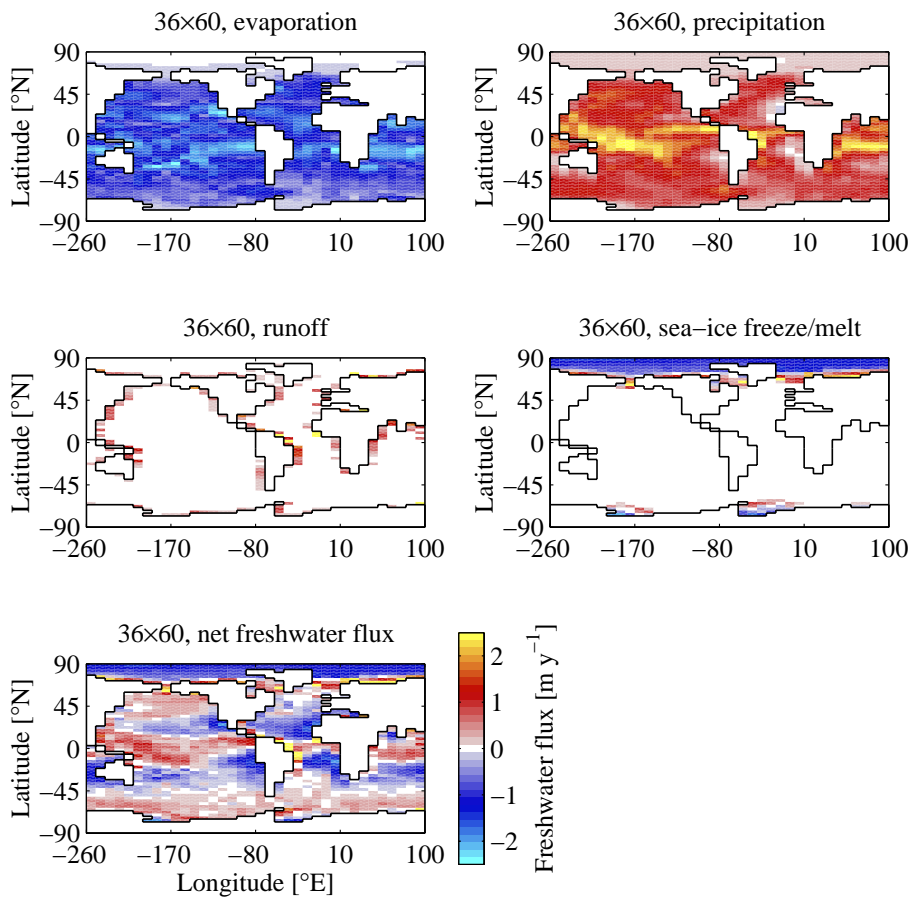


Fig. 30. Maps of annual-mean components of freshwater flux into the ocean, m y^{-1} (36×60 mesh).

The “genie_eb_gogs” configuration of GENIE

R. Marsh et al.

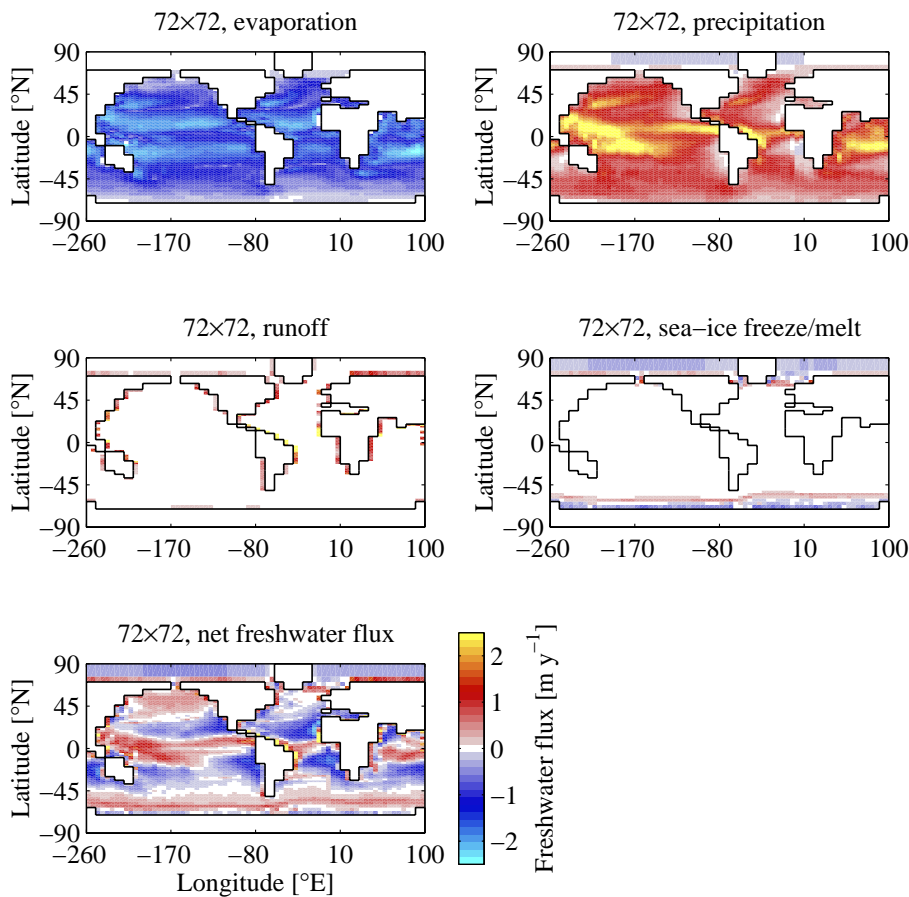


Fig. 31. Maps of annual-mean components of freshwater flux into the ocean, m y^{-1} (72x72 s mesh).

- [Title Page](#)
- [Abstract](#) [Introduction](#)
- [Conclusions](#) [References](#)
- [Tables](#) [Figures](#)
- [◀](#) [▶](#)
- [◀](#) [▶](#)
- [Back](#) [Close](#)
- [Full Screen / Esc](#)
- [Printer-friendly Version](#)
- [Interactive Discussion](#)



The “genie_eb_gos” configuration of GENIE

R. Marsh et al.

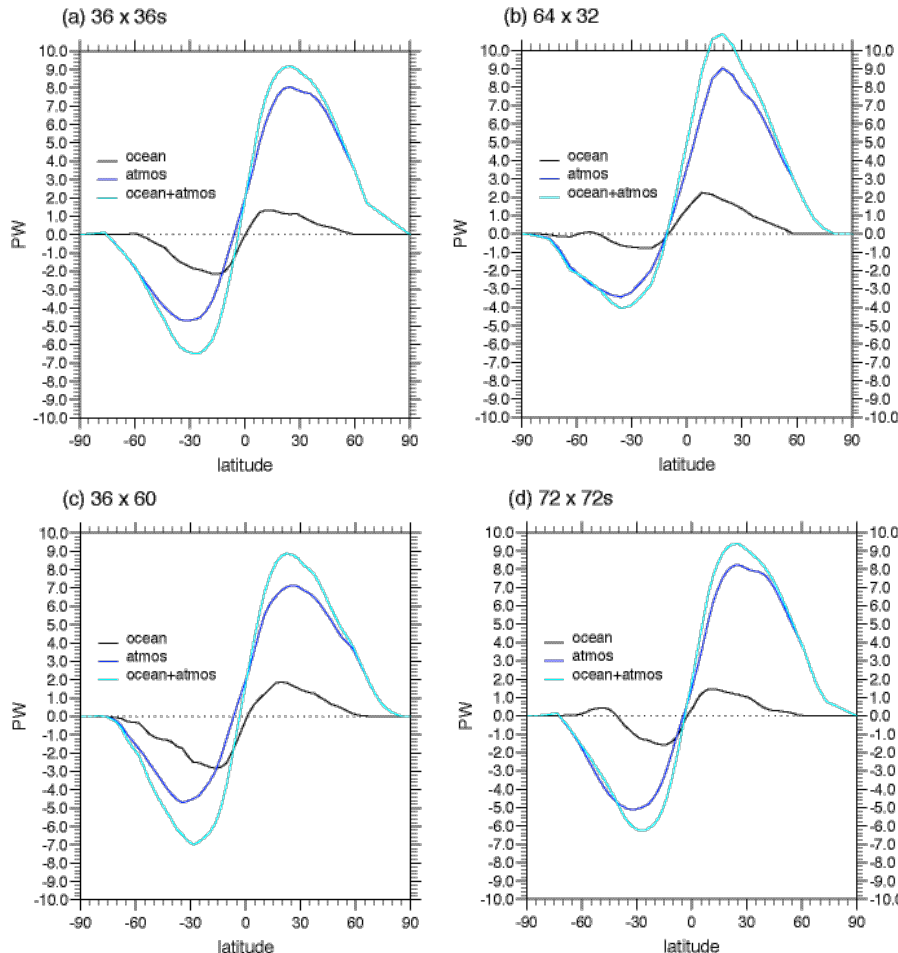


Fig. 32. Meridional heat transports (oceanic, atmospheric, total, PW).

[Title Page](#)

[Abstract](#)

[Introduction](#)

[Conclusions](#)

[References](#)

[Tables](#)

[Figures](#)

◀

▶

◀

▶

[Back](#)

[Close](#)

[Full Screen / Esc](#)

[Printer-friendly Version](#)

[Interactive Discussion](#)

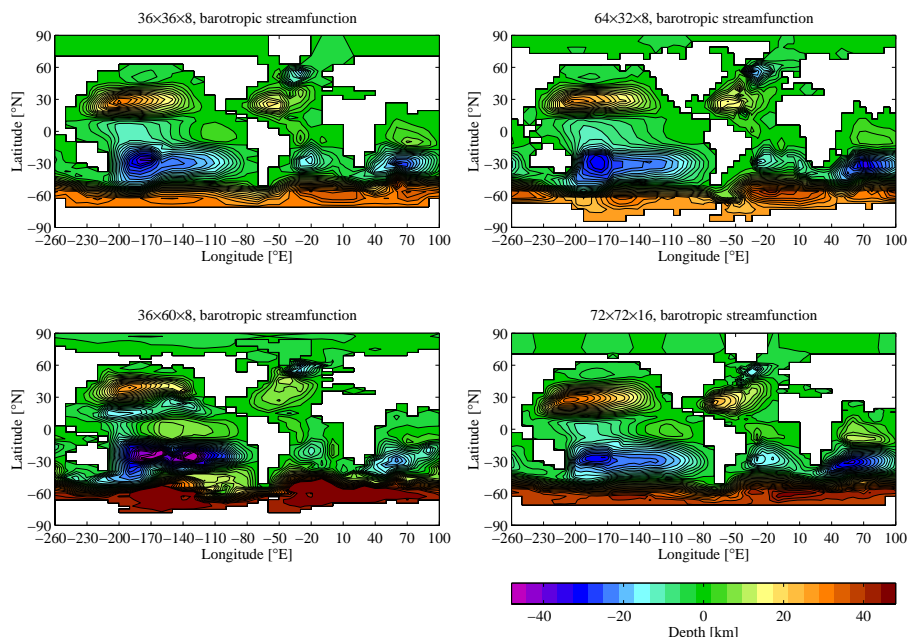


Fig. 33. Barotropic streamfunctions (Sv).

The “genie_eb_go_gs” configuration of GENIE

R. Marsh et al.

[Title Page](#)

[Abstract](#)

[Introduction](#)

[Conclusions](#)

[References](#)

[Tables](#)

[Figures](#)

◀

▶

◀

▶

[Back](#)

[Close](#)

[Full Screen / Esc](#)

[Printer-friendly Version](#)

[Interactive Discussion](#)



The “genie_eb_gs” configuration of GENIE

R. Marsh et al.

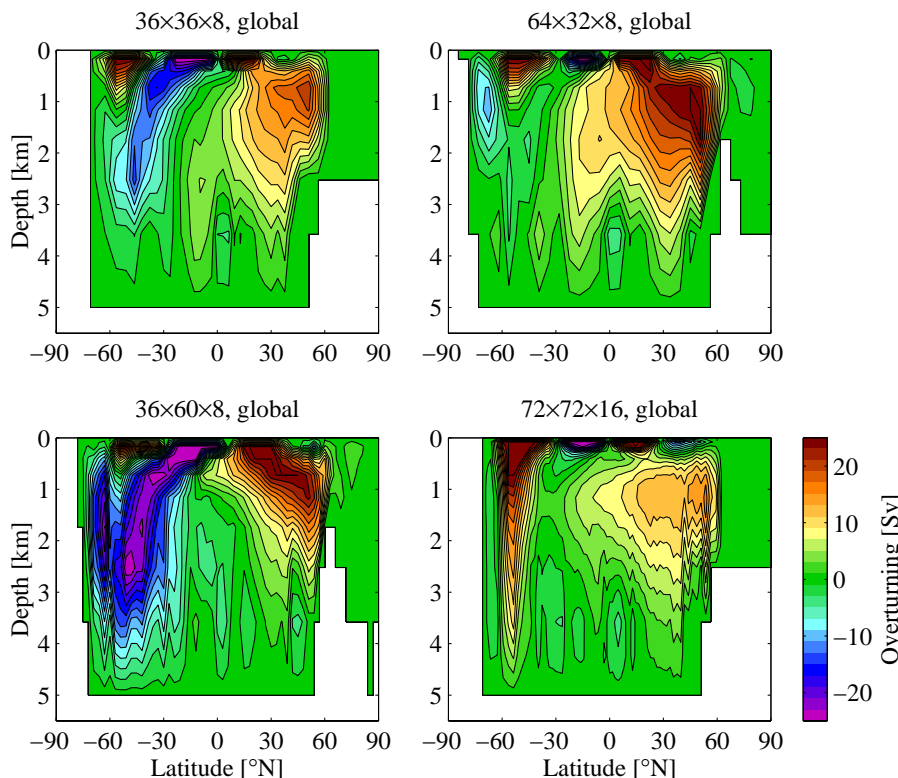


Fig. 34. Meridional overturning streamfunctions (Sv) for Global Ocean.

[Title Page](#)

[Abstract](#)

[Introduction](#)

[Conclusions](#)

[References](#)

[Tables](#)

[Figures](#)

[◀](#)

[▶](#)

[◀](#)

[▶](#)

[Back](#)

[Close](#)

[Full Screen / Esc](#)

[Printer-friendly Version](#)

[Interactive Discussion](#)



The “genie_eb_gos” configuration of GENIE

R. Marsh et al.

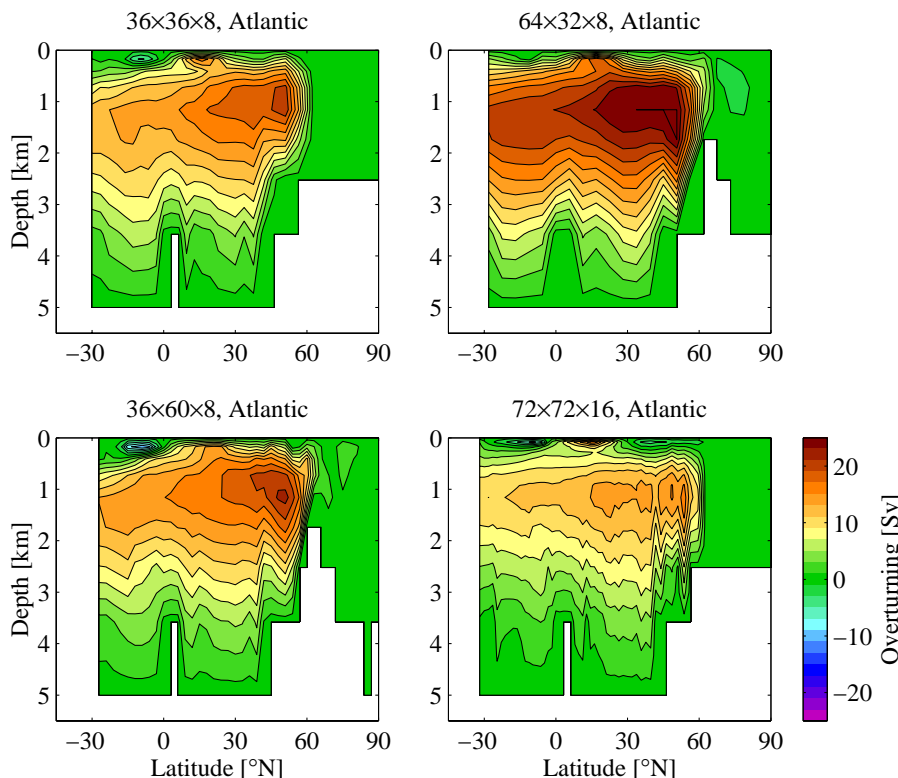


Fig. 35. Meridional overturning streamfunctions (Sv) for Atlantic Ocean.

[Title Page](#)

[Abstract](#)

[Introduction](#)

[Conclusions](#)

[References](#)

[Tables](#)

[Figures](#)

[◀](#)

[▶](#)

[◀](#)

[▶](#)

[Back](#)

[Close](#)

[Full Screen / Esc](#)

[Printer-friendly Version](#)

[Interactive Discussion](#)



The “genie_eb_gos” configuration of GENIE

R. Marsh et al.

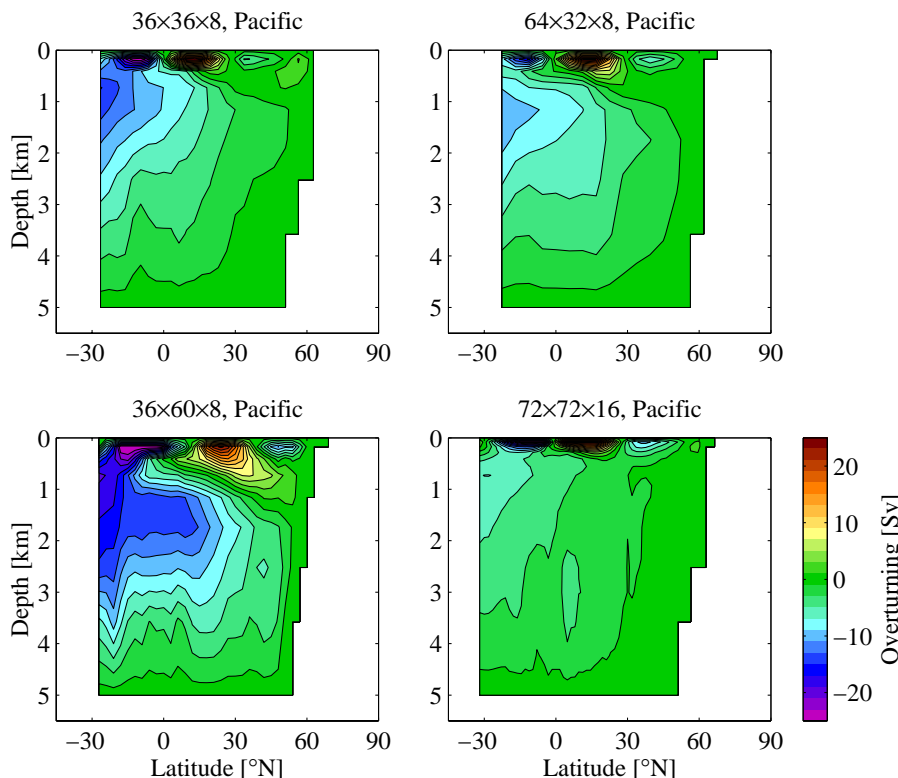


Fig. 36. Meridional overturning streamfunctions (Sv) for Pacific Ocean.

[Title Page](#)

[Abstract](#)

[Introduction](#)

[Conclusions](#)

[References](#)

[Tables](#)

[Figures](#)

[◀](#)

[▶](#)

[◀](#)

[▶](#)

[Back](#)

[Close](#)

[Full Screen / Esc](#)

[Printer-friendly Version](#)

[Interactive Discussion](#)



The “genie_eb_gs” configuration of GENIE

R. Marsh et al.

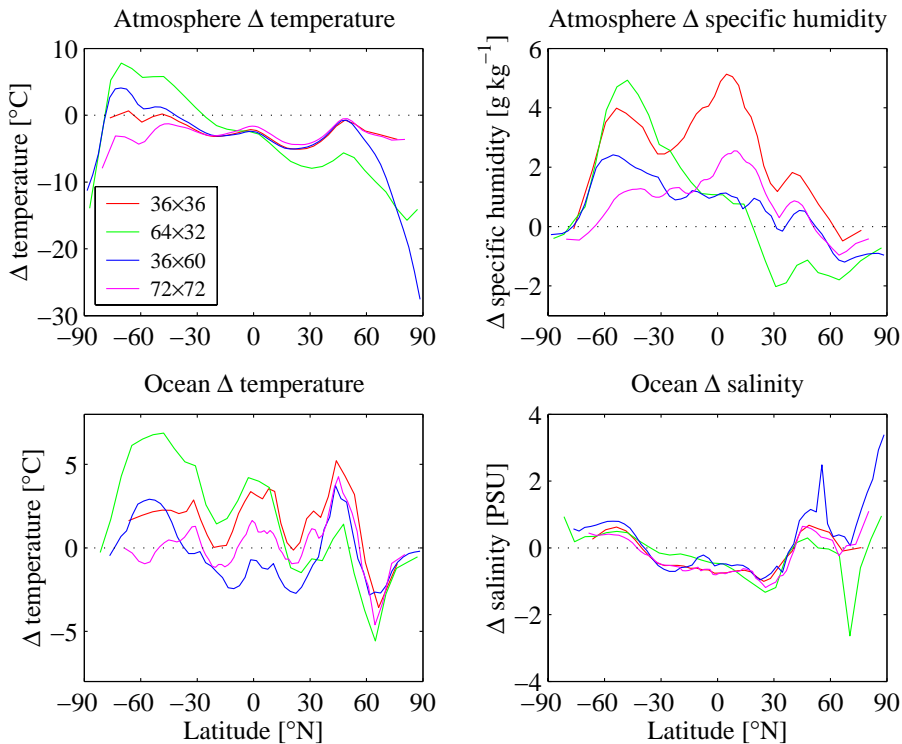


Fig. 37. Annual-mean “model minus observation” differences of zonally-averaged air temperature ($^{\circ}\text{C}$), specific humidity (g kg^{-1}), sea surface temperature ($^{\circ}\text{C}$) and sea surface salinity (psu). Atmospheric observations are from the NCEP/NCAR reanalysis. Ocean observations are the Levitus et al. (1998) climatology.

[Title Page](#)

[Abstract](#)

[Introduction](#)

[Conclusions](#)

[References](#)

[Tables](#)

[Figures](#)

[◀](#)

[▶](#)

[◀](#)

[▶](#)

[Back](#)

[Close](#)

[Full Screen / Esc](#)

[Printer-friendly Version](#)

[Interactive Discussion](#)

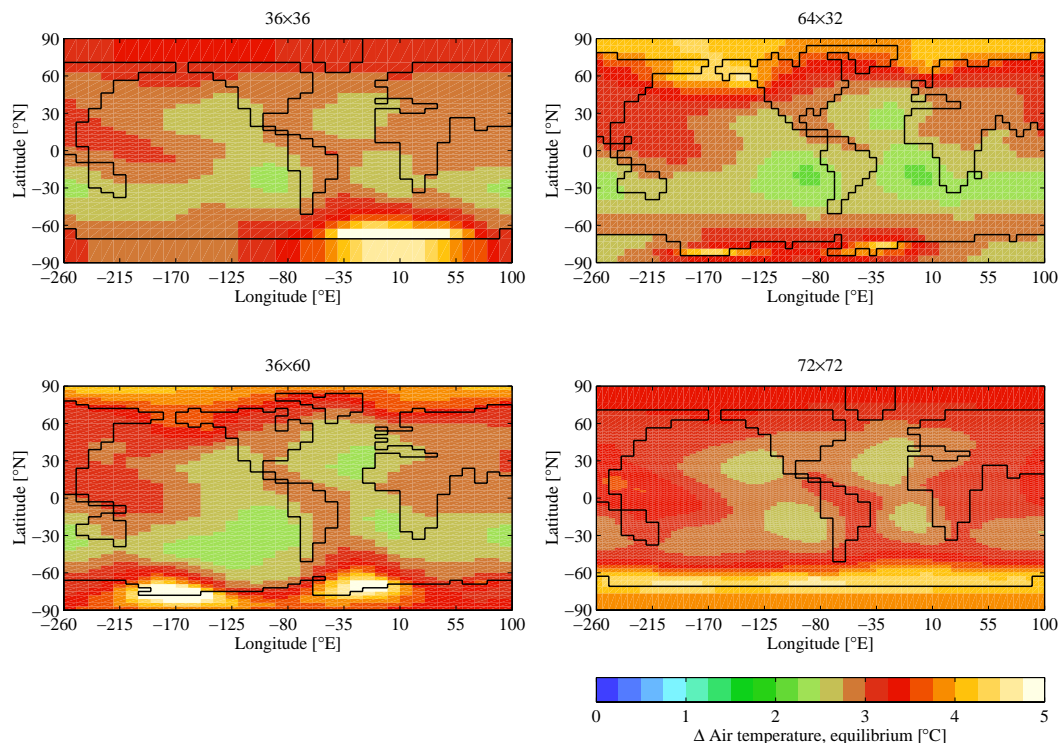


Fig. 38. Maps of change of air temperature ($^{\circ}$ C) from the equilibrium climate sensitivity experiments: $2\times\text{CO}_2-1\times\text{CO}_2$.

The “genie_eb_gos” configuration of GENIE

R. Marsh et al.

[Title Page](#)

[Abstract](#)

[Introduction](#)

[Conclusions](#)

[References](#)

[Tables](#)

[Figures](#)

◀

▶

◀

▶

[Back](#)

[Close](#)

[Full Screen / Esc](#)

[Printer-friendly Version](#)

[Interactive Discussion](#)

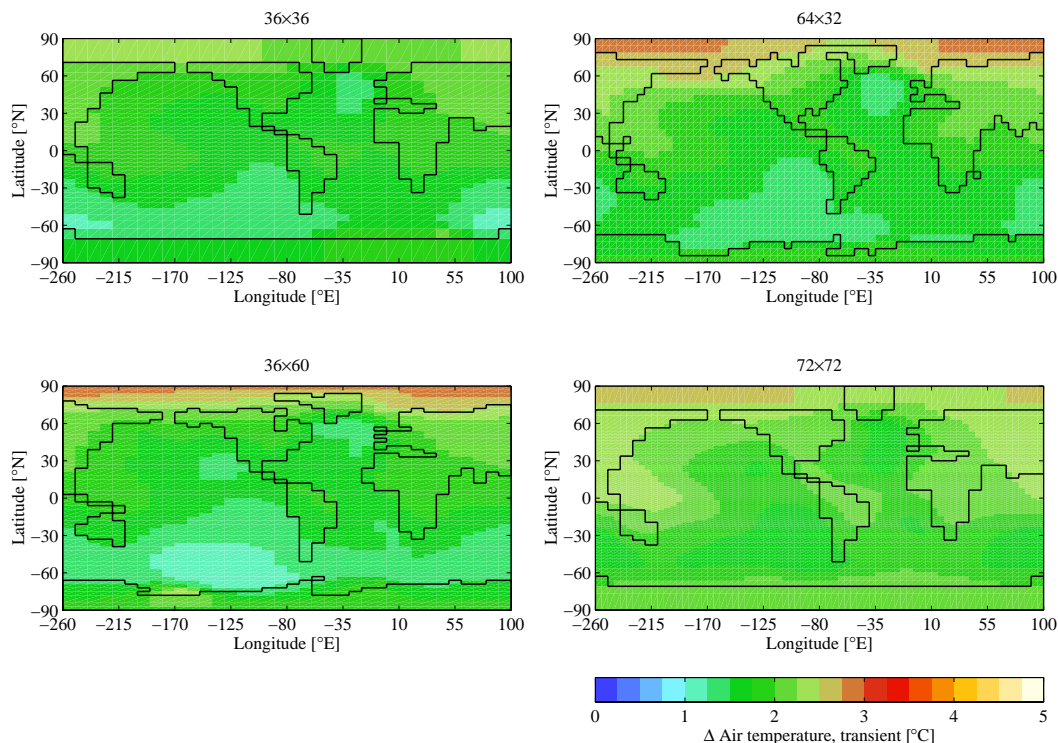


Fig. 39. Maps of change of air temperature ($^{\circ}\text{C}$) from the transient climate response experiments: on CO_2 doubling, at 1% per annum increase.

The “genie_eb_go_gs” configuration of GENIE

R. Marsh et al.

[Title Page](#)

[Abstract](#)

[Introduction](#)

[Conclusions](#)

[References](#)

[Tables](#)

[Figures](#)

◀

▶

◀

▶

[Back](#)

[Close](#)

[Full Screen / Esc](#)

[Printer-friendly Version](#)

[Interactive Discussion](#)

The “genie_eb_go_gs” configuration of GENIE

R. Marsh et al.

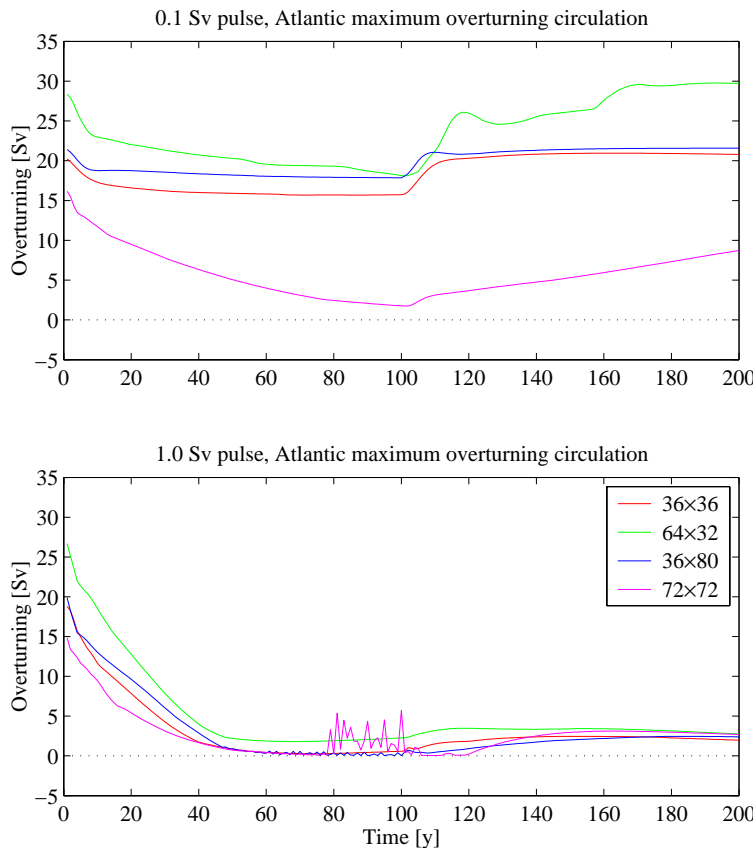


Fig. 40. Maximum and minimum AMOC intensity (Sv) during the freshwater hosing experiments, with constant freshwater addition for 100 years: (a) at 0.1 Sv; (b) 1.0 Sv.

- [Title Page](#)
- [Abstract](#) [Introduction](#)
- [Conclusions](#) [References](#)
- [Tables](#) [Figures](#)
- [◀](#) [▶](#)
- [◀](#) [▶](#)
- [Back](#) [Close](#)
- [Full Screen / Esc](#)
- [Printer-friendly Version](#)
- [Interactive Discussion](#)

The “genie_eb_gogs” configuration of GENIE

R. Marsh et al.

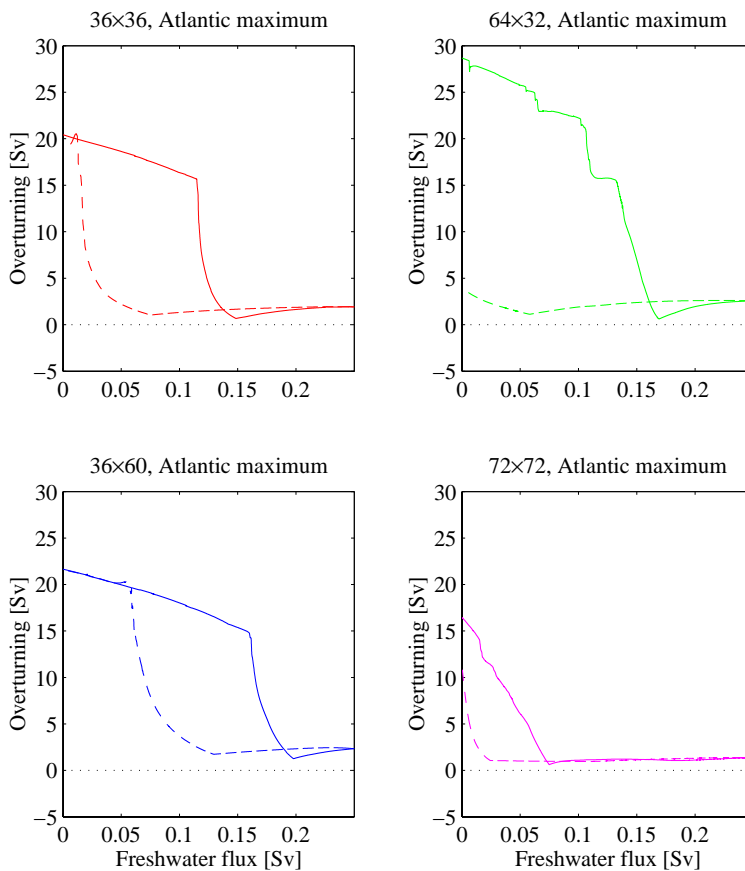


Fig. 41. AMOC hysteresis loop, showing AMOC intensity (Sv) as a function of increasing and decreasing freshwater hosing at 0.05 Sv per 1000 years: **(a)** 36×36 s; **(b)** 64×32; **(c)** 36×60; **(d)** 72×72 s.

[Title Page](#)

[Abstract](#)

[Introduction](#)

[Conclusions](#)

[References](#)

[Tables](#)

[Figures](#)

[◀](#)

[▶](#)

[◀](#)

[▶](#)

[Back](#)

[Close](#)

[Full Screen / Esc](#)

[Printer-friendly Version](#)

[Interactive Discussion](#)